Chapter 5
NSTX-U Contributions to the FY2013 Joint Research Target

S.P. Gerhardt[1], R Maingi[1], D. Battaglia[1], R.E. Bell[1], J.M. Canik[2], N. Crocker[3], A. Diallo[1], R. Goldston[1], S. Kubota[3], B.P. LeBlanc[1], S. Parker[4], Y. Ren[1], F. Scotti[1], D.R. Smith[5], P. Snyder[6], K. Tritz[7], W. Wan[4]

[1]Princeton Plasma Physics Laboratory, Plainsboro, NJ, USA
[2]Oak Ridge National Laboratory, Oak Ridge, TN, USA
[3]Department of Physics and Astronomy, University of California, Los Angeles, USA
[4]Department of Physics, University of Colorado, Boulder, USA
[5]Department of Engineering Physics, University of Wisconsin-Madison, USA
[6]General Atomics, San Diego, CA, USA
[7]Department of Physics and Astronomy, Johns Hopkins University, Baltimore, MD, USA

1.0 Overview

1.1: The need for stationary confinement regimes without large ELMs

The H-mode confinement regime is characterized by a strong thermal and particle transport barrier at the plasma edge, known as the H-mode pedestal. The excellent thermal confinement is beneficial for fusion systems, but the excellent particle transport can result in unacceptable impurity accumulation. This transport barrier is often interrupted in periodic MHD events knows as Edge Localized Modes (ELMs). ELMs have the beneficial result of flushing impurities from the plasma core, enabling stationary conditions. However, the impulsive thermal loading due to natural ELMs will severely limit the divertor lifetime in next step devices such as ITER.

In order to address this apparent conflict for ITER, a number of approaches are under considerations [1]. One approach is the trigger ELMs much more rapidly than their natural rate, which should reduce the magnitude of the impulsive heat flux. The primary ELM pacing techniques for ITER are likely to be pellet pacing [1,2-6] or triggering via "vertical jogs" [1,7-12]. These methods have been shown to reduce the impulsive heat fluxes while providing the required impurity transport. Alternatively, the application of resonant magnetic perturbations (RMP) has been shown to suppress ELMs in DIII-D [1,13-15]; the physics of RMP is still under active investigation, but may be related to some mechanism that limits the radial expansion of the H-mode pedestal [16].

In addition to these regimes of active ELM control, there is considerable interest in plasma regimes where intrinsic fluctuations replace ELMs for particle control, with minimal impulsive heat flux. Examples of these regimes include the Quiescent H-mode (QH-mode), discovered and optimized in DIII-D [17-21] and since duplicated in JET [22], JT-60 [23,24] and ASDEX-Upgrade [22,25] or the I-mode, first observed in ASDEX-Upgrade [26] and systematically explored and exploited in Alcator C-Mod [27-31]. In the case QH-mode, the intrinsic fluctuations are known as the Edge Harmonic Oscillations (EHO), and are believed to be saturated peeling instabilities. In the I-mode, the intrinsic fluctuations are referred to as the Weekly Coherent Mode (WCM). These regimes, with levels of thermal confinement comparable or exceeding that in H-mode, acceptable particle transport facilitating stationary conditions, and no large ELMs, are a primary subject of the 2013 OFES Joint Research Target.

1.2: The 2013 OFES Joint Research Target

Given the critical issues described in the previous section, the 2013 OFES Joint Research Target (JRT) has been formulated. The goals of this research are described in the annual target and the 4th quarter milestone descriptions:

Annual Target:

Conduct experiments and analysis on major fusion facilities, to evaluate stationary enhanced confinement regimes without large Edge Localized Modes (ELMs), and to improve understanding of the underlying physical mechanisms that allow acceptable

edge particle transport while maintaining a strong thermal transport barrier. Mechanisms to be investigated can include intrinsic continuous edge plasma modes and externally applied 3D fields. Candidate regimes and techniques have been pioneered by each of the three major US facilities (C-Mod, D3D and NSTX). Coordinated experiments, measurements, and analysis will be carried out to assess and understand the operational space for the regimes. Exploiting the complementary parameters and tools of the devices, joint teams will aim to more closely approach key dimensionless parameters of ITER, and to identify correlations between edge fluctuations and transport. The role of rotation will be investigated. The research will strengthen the basis for extrapolation of stationary regimes which combine high energy confinement with good particle and impurity control, to ITER and other future fusion facilities for which avoidance of large ELMs is a critical issue.

4th Quarter Milestone:

Complete the required experiments and analysis. Prepare a joint report summarizing the contributions toward the development high-performance stationary regimes devoid of large ELMs, and identifying important paths for future exploration.

This document fulfills the NSTX-U portion of the 4th quarter milestone, and represents the NSTX-U contribution to the 2013 JRT.

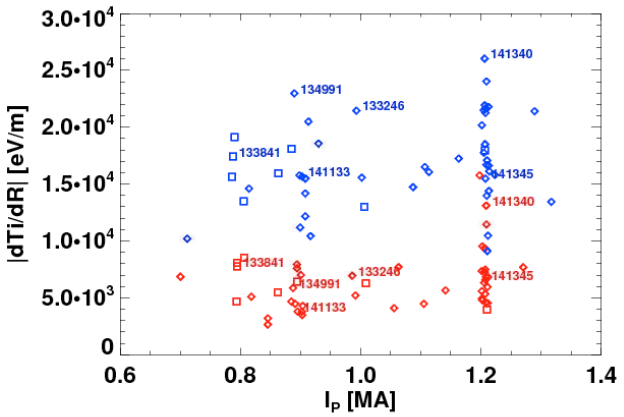

Fig. 5.1: Inverse ion temperature scale length for EP H-mode (blue) and H-mode (red) examples in NSTX.

1.3: NSTX-U contributions to the 2013 Joint Research Target

NSTX did not have regimes that strictly satisfy these goals of the JRT; the density typically ramps in essentially all NSTX discharges. Hence, the NSTX-U contribution addresses sub-components of the JRT goals:

- Section 2.0 addresses the Enhanced Pedestal H-mode (EP H-mode) [32-33]. This regime shows a separation between particle and thermal transport, similar to other regimes of interest for the JRT, and may be a candidate for high-performance operation in NSTX-U and nest-step STs. Pedestal dynamics, transport, and fluctuations in this regime are discussed, as are issues associated with controlling access to the EP H-mode configuration.
- Section 3.0 discusses ELM-free regimes produced via lithium PFC conditioning [34]. This section describes both the impurity dynamics [35] and the fluctuation scaling [36] in these regimes.

- Section 4.0 describes the observations of edge harmonic oscillations in NSTX [37,38] These oscillations are similar to those observed during QH-mode operation in DIII-D, though they do not contribute to particle transport in any meaningful way, apparently due to their low amplitude. The structure of these modes in NSTX is discussed, using data from reflectometers, beam emission spectroscopy, and soft X-rays. Methods to potentially drive these oscillations to large amplitude in NSTX-U are discussed.

2.0 Enhanced Pedestal H-mode Research

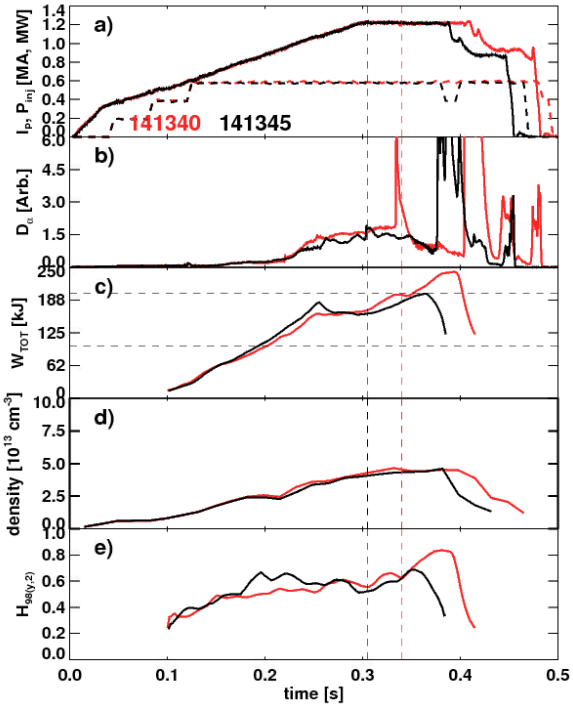

Fig. 5.2: Time evolution of short-lived EP H-mode example discharges. Shown are a) the plasma current and beam power, b) the divertor D_a emission, c) the stored energy, d) the line averaged density, and e) the confinement multiplier $H_{98(y,2)}$.

As noted in section 1, the Enhance Pedestal H-mode [32,33] is a potentially attractive confinement regime for next step-ST plasmas. It is defined by the following characteristics:

- There is a discreet transition to this confinement regime, with this transition always following the L->H transition. This transition is often, but not always, triggered by an ELM.

- There is a region in the plasma edge with very sharp ion temperature gradients. This is illustrated in Fig. 5.1, where the normalized ion temperature gradient is shown as a function of plasma current for the H-mode and EP H-mode phases for a large database of discharges. The gradients in the EP H-mode phases are typically a factor of 3 larger than those in the H-mode phase.

- There is a localized region of large rotation shear in the plasma edge, in the vicinity of the steep ion temperature gradient. There is often, but not always, a local minima in the rotation.

2.1: General EP H-mode Characteristics

2.1.1: Early EP H-mode Transition Examples

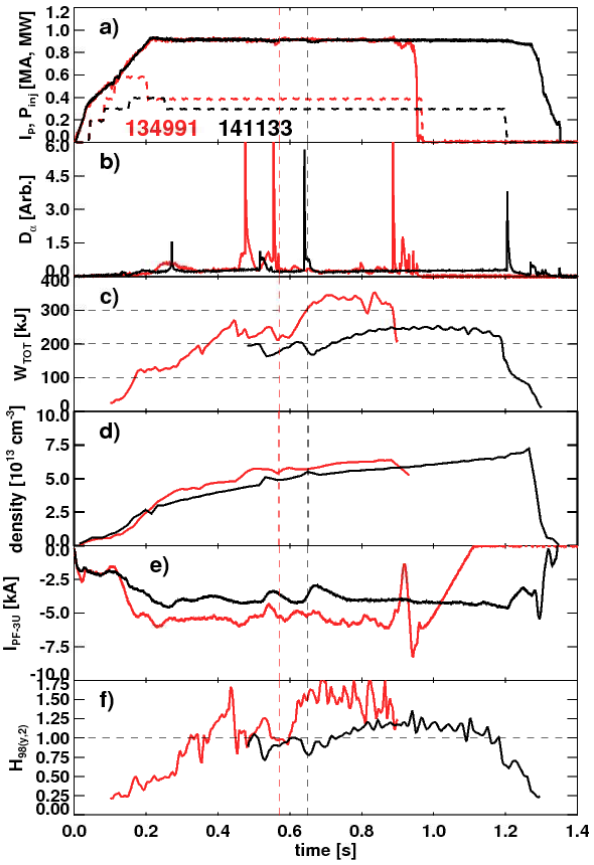

Fig. 5.3: Time evolution of long-pulse EP H-mode example discharges. Shown are a) the plasma current, b) the divertor D_a emission, c) the stored energy, d) the line-average density, e) the current in the radial field coil, and f) the $H_{98(y,2)}$ confinement multiplier.

The first EP H-mode examples in NSTX [32] were typically rather short lived, with durations of less than 100 ms. In these cases, the transition to EP H-mode typically occurred either during the current ramp or early in the flat-top phase. Recent examples the time evolution of these cases can be found in Fig. 5.2, for a pair of I_P=1.2 MA discharges; these discharges were made during the 2010 run campaign in order to study EP H-mode plasmas. In both cases, the H-mode transition occurs at t=0.215 s, as indicated by the sharp change in slope of the density evolution. In 141340, the EP H-mode transition occurs following a large ELM, as has often been observed. However, in 141345, no large ELM is observed, demonstrating that these regimes can be initiated without an ELM. There is a strong ramp in the stored energy, indicating the improved confinement. The confinement multiplier $H_{98(y,2)}$ also shows a ramp at this time, though the discharge disrupts before the confinement can reach a high level. There is a small ramp in the line-average density during this phase. These short pulse examples indicate the potential benefits of the regime, motivating the search for other examples.

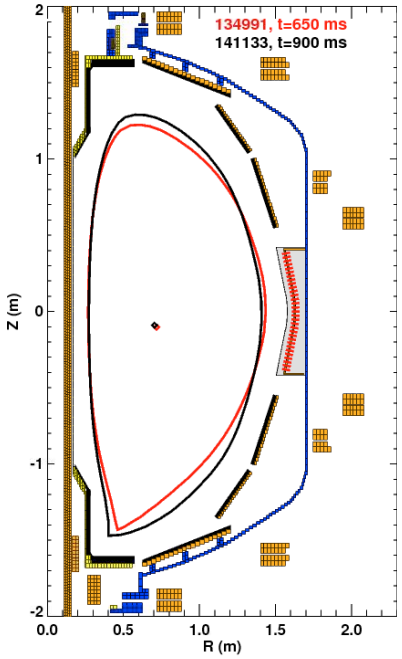

Fig. 5.4: Typical separatrix shapes for the long-pulse EP H-mode examples.

2.1.2: Long-Pulse EP H-Mode Examples

More recently, long-pulse EP H-mode examples have been observed. The Fig. 5.3 shows examples of these cases including discharge 134991 in red discussed in Ref. [33] and the newly observed discharge 134333. As indicated in frame a), both are I_P=900 kA discharges, heated by either 3 or 4 MW of neutral beam injection. The vertical lines indicate the time of transition to EP H-mode, which follows an ELM is both cases. There are large increments in stored energy following the transition, and both examples show a plateau in the stored energy for many confinement times. Indeed, while 134991 eventually suffers a disruption, potentially associated with the q=1 surface entering the plasma, discharge 141133 maintains a high confinement state for the duration of the heating power application. The discharge 134991 achieves very high $H_{98(y,2)}$ factors of ~1.5, while 141133 has the still impressive $H_{98(y,2)}$ factor of 1.2. Unfortunately, the density does increase during the EP H-mode phase of these discharges.

The boundary shapes for these two examples are shown in Fig. 5.4. Discharge 134991 is a moderate triangularity discharge δ_l=0.63 , while discharge 141133 has a high value of triangularity δ_l=0.8. More importantly, the EP H-mode phase of 141133 is extremely quiescent compared to other H-mode discharges. This is visible in the stored energy trace, or in the PF-3U coil current in Fig. 5.3. This coil controls both the elongation and vertical position of the plasma via feedback loops. The steady nature of that coil current indicates the lack of transients in the discharge, a characteristic highly desirable for next step configurations.

2.1.3: Typical Profile Shapes and Evolution

As part of the 2013 JRT analysis, a small code was written to identify discharges with very steep gradients in the ion temperature, with the expectation that this would identify additional EP H-mode examples. This was indeed the case, with the number of identified EP H-mode discharge increasing by many factors. More interestingly, this exercise revealed that there is a large range of T_i profile shapes that may be considered within the bounds of the enhanced pedestal H-mode. Examples of these profile shapes are illustrated in Fig. 5.5. Note that these discharges occurred on different experimental run days, and only discharge 141340 was executed with the intention of studying EP H-modes.

In this figure, the top row shows the electron and on temperatures, along with both tanh fits to T_i and a line tangent to the point of the maximum T_i gradient. The tanh fit is defined via the function:

$$Y(X) = Y_{offset} + \frac{\left(Y_{pedestal} - Y_{offset}\right)\left(1 + 0.5\alpha_{slope} z\right)}{1 + e^{-2z}},$$

with $z=2(X_{symmetry}-X)/\Delta_{width}$ [39]. Here, Y can represent T_e, T_i, n_e or any other profile quantity, while X can represent either outboard midplane major radius or some flux surface label such as normalized poloidal flux. Y_{offset}, $Y_{pedestal}$, α_{slope}, $X_{symmetry}$, and Δ_{width} are fit parameters determined by a non-linear fitting routine.

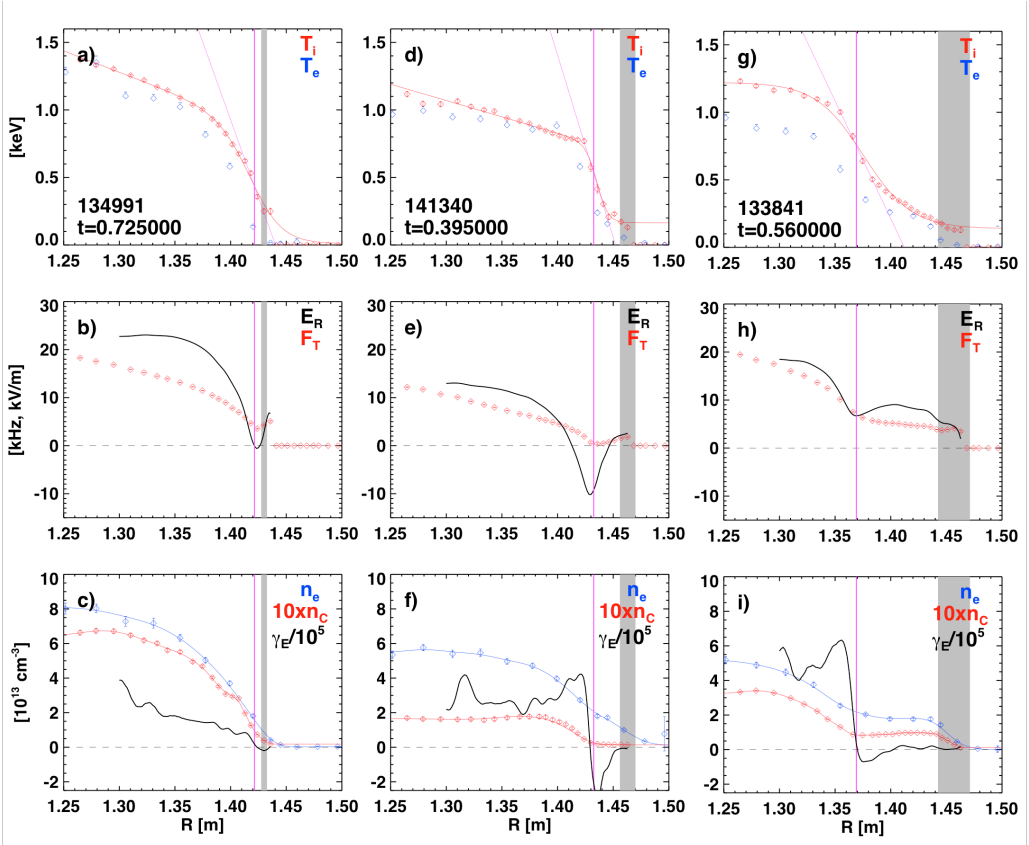

Fig. 5.5: Examples of profile shapes during EP H-mode in NSTX. The top frame of each column shows the ion and electron temperature profiles. The points show the data, while the lines show tanh fits, the magenta line marks to location of maximum ion temperature gradient and the tangent line to the profile at that point. The middle frames show the toroidal rotation and radial electric field profiles (computed neglecting the poloidal rotation), while the bottom frames show the electron and carbon density, as well as the ExB shearing rate. The grey shaded regions indicate the approximate regions of the separatrix.

The second row shows the toroidal rotation profile, as well as the E_R profile evaluated from the measured carbon parameters as $E_R = \frac{1}{6eN_C}\frac{dP_C}{dR} + V_T B_P$. The poloidal rotation, which is generally small in NSTX [40], is neglected in this calculation; this assumption must be validated in future research evaluating the poloidal rotation in this region. The radial electric field so calculated is then used to calculate the ExB shearing rate in the bottom frames, as [41] $\gamma_E = \left(\frac{r}{q}\right)\frac{d}{dr}\left(\frac{E_R}{RB_P}\right)$. The bottom row also shows the electron and scaled carbon density profiles, along with spline fits to those profiles. The separatrix location is shown as the gray shaded region, determined by the values give by equilibrium reconstruction, the T_e=40 eV location, and the T_e=80 eV location.

The left-most column of Fig. 5.5 shows the edge profiles for the long-pulse EP H-mode discharge 134991, whose time evolution is illustrated in Fig. 5.3. In this case, the region of steep T_i gradient is very close to the plasma edge. There is a clear minima in the

rotation profile, with a deep E_R well developing. The profiles for the other long-pulse discharge in Fig. 5.3 (141133) are of similar shape, and will be illustrated below.

The middle column of Fig. 5.5 shows the profiles for a case typical of the short-lived EP H-modes that transition before or just after the start of the I_P flat-top; see Fig. 5.2 for the time evolution of 0D quantities in this case. In this example, the region with the steepest T_i gradient is shifted in a few cm, with a clear region of lower T_i gradient farther outside. However, the clear rotation profile minima and E_R well are still present.

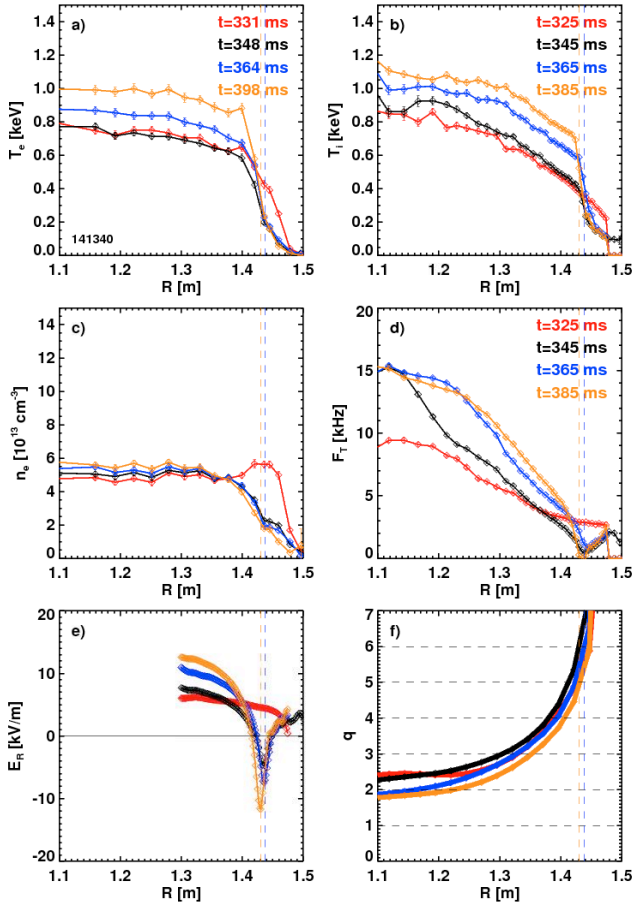

Fix. 5.6: Time evolution of the profiles from EP H-mode discharge 141340, snap-shots from which are shown in the center column of Fig. 5.5. Shown are profiles of the a) the electron temperature, b) the ion temperature, c) the electron density, d) the toroidal rotation, e) the radial electric field, and f) the safety factor.

Finally, the right most column shows a case where the steep T_i gradient is shifted inward ~10 cm from the plasma edge. There is an associated inward shift of the region of sharp rotation gradient indicating that the relationship between the steep ion temperature gradient and rotation is maintained. In this case, both T_e and n_e show a double-barrier structure, and the configuration could be called a wide radius internal transport barrier (ITB) or an EP H-mode. For this reason, cases such as in the right column of Fig. 5.5 will be noted with a square in the scatter plots below, whereas cases such as in the left and center column will be denoted with a diamond.

The profile evolution for the example in the center column of Fig. 5.5 is shown in Fig. 5.6; this is the high-current example transitioning to EP H-mode early in the discharge. The CHERS data (F_T, T_i, E_R) and MPTS data (T_e, n_e) are on slightly different time bases, so nearly synchronous samples are indicated with the same color. At t=330ms, the configuration is in H-mode, with broad density, temperature and rotation profiles. The edge T_i pedestal is not resolved by the CHERS diagnostic, and so the E_R features at the edge are not fully resolved.

After t=330 ms, the EP H-mode transition occurs following a large ELM, with a number of associated changes in the profiles. The electron density and temperature at the plasma edge are reduced, and the rotation immediately develops a local minima. The ion temperature at the very edge is also transiently reduced, though the core ion temperature is largely unchanged; this results in a region of sharp T_i gradient at the location where the two regions connect. These rotation and pedestal dynamics result in the formation of a deep well in the E_R profile.

From that point onward, the minima in the rotation remains, marked by vertical dashed lines in the figure for the later time slices. The width of the ion temperature pedestal increases at roughly fixed gradient scale length until the EP H-mode phase ends with a disruption. Note the double hump structure in the density, barely visible in the bottom, center frame of Fig. 5.5, but clearly visible in Fig. 5.6c).

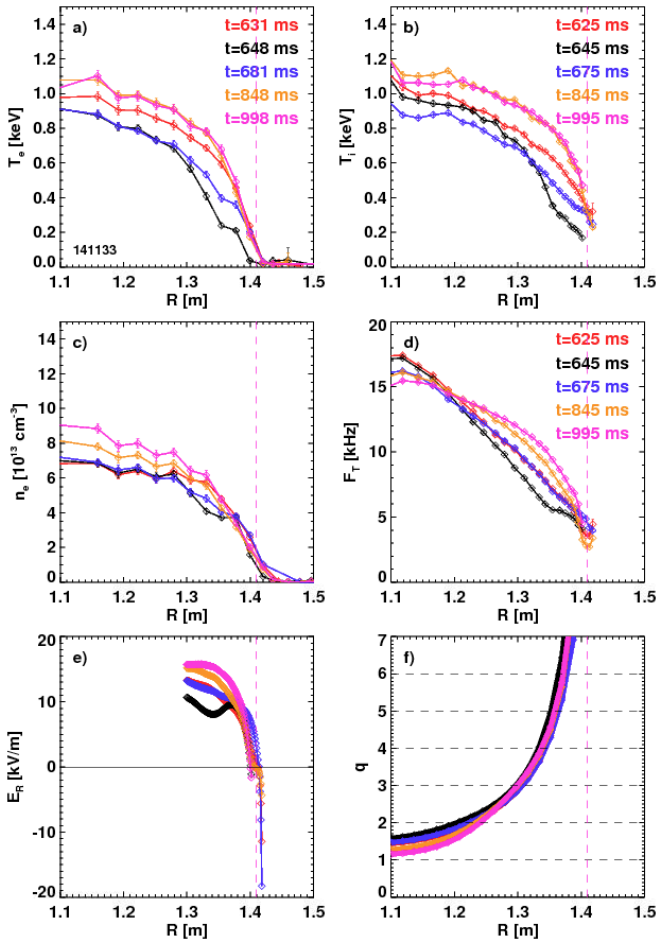

Fig. 5.7: Profile evolution for the long pulse EP H-mode discharge 141133. The frames are the same as in Fig. 5.6.

It has been speculated that the minima in the rotation profile is associated with a single rational surface [Maingi 2010]. However, as illustrated in Fig.5.6f), isolating which surface would play this role has proven difficult. This figure shows the q profile at the time of interest, with the vertical lines indicating where a rational surface might be anticipated. The minima in the rotation appears to not be located at the q=2, 3, or 4 surfaces. It may be located at one of the q>4 surfaces, though isolating which one is essentially not possible due to the large magnetic shear.

Fig. 5.7 shows the profile evolution for the recently discovered long-pulse EP H-mode discharge 141133. This case does not have as steep an ion temperature gradient at the discharge in Fig. 5.6. However, as shown in Fig. 5.1, the edge T_i gradient is still well above the levels of typical H-mode plasmas.

As observed in the previous example, the ELM that triggers the EP H-mode transition results in a drop in the edge ion temperature, while leaving the core value unchanged (compare black and red curves). The ion temperature then recovers, ultimately developing a very steep profile at the plasma edge. The rotation profile shows hints of a local minima at the edge for some time slices. However, the CHERS diagnostic is unable to reliably make measurements towards the bottom of the pedestal, and so it is difficult to assess if this feature is constant in time.

Finally, Fig. 5.8 shows the profile evolution for a discharge with the region of steepest ion temperature gradient shifted inwards. This is a discharge with triggered ELMs [42-44]; there are a number of small ELMs in the vicinity of the transition to the EP H-mode line state, although it is difficult to identify which, if any, play a role in triggering the transition. In any case, the transition is again initiated by a drop in the edge ion temperature, resulting in a region of steep T_i gradient. The width of the region then grows at roughly fixed gradient.

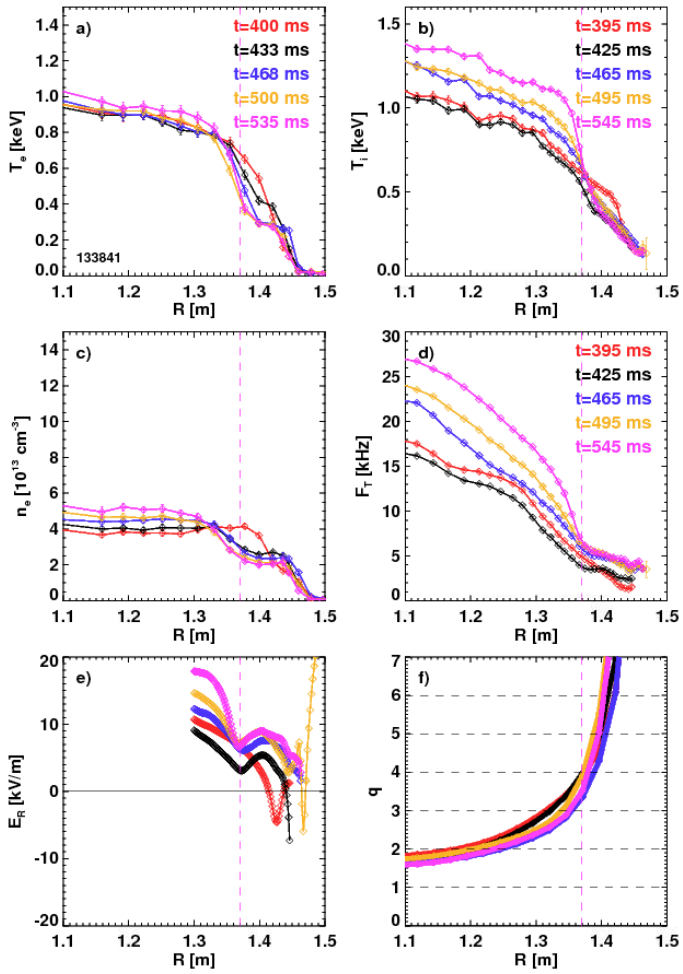

Fig. 5.8: Profile evolution for the EP H-mode example 133841, where the region of steep T_i gradient is shifted inward. The frames are the same as in Fig. 5.6, though the scales differ.

The unique dynamics of this configuration also manifest themselves in the other profiles. The electron density and temperature begins to develop a double-barrier shape immediately following the transition, and this shape is maintained throughout the EP H-mode like phase. The toroidal rotation profile in the H-mode phase is fairly broad, and shows a rapid drop at the EP H-mode transition. The rotation gradient then builds rapidly, staying aligned with the region of steep T_i gradient. Note that the H-mode profiles have a strong E_R well, but the EP H-mode like profiles show significant E_R shear developing well inside the plasma.

Figures 5.5-5.8 also make important points with regard to 1) potential 3D variations and 2) rotation profile shapes.

With regard to potential 3D perturbations to the equilibria,

it is noted at that there is often a substantial radial distance (2-5cm) between the regions of steep T_e and T_i gradients; this can be easily observed from comparing frames a) and b) of Fig. 5.6 and 5.7, using the vertical lines as guides. Given that the T_e and T_i profiles are measured with diagnostics whose toroidal separation is 180°, this might imply that there are significant 3D distortions to the plasma. This separation is typically not observed in H-mode plasmas, indicating that it is not related to diagnostic spatial calibration issues. Further suspicion may arise from comparisons of the q-profile, derived from intrinsically axisymmetric solutions to the Grad-Shafranov equation, with the toroidally localized CHERS measurements: the locations of minima appear to be in very high shear regions, and not in the vicinity of the low-n resonant surfaces initially considered important for this damping. However, there are a number of observations that point away from a 3D solution:

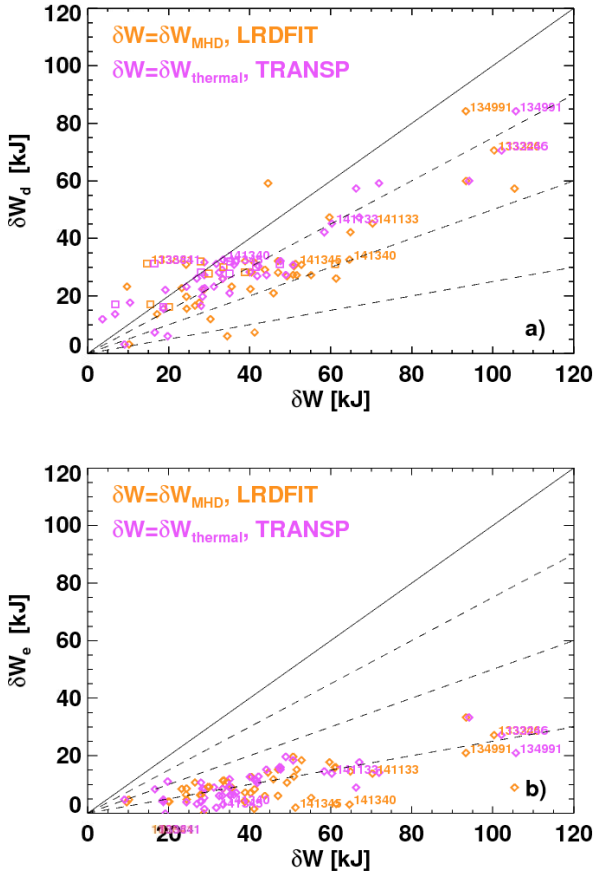

Fig 5.9: Increments of the deuterium (top) and electron (bottom) stored energy, as a function of the total stored energy increment δW. The orange points are based on calculating δW from equilibrium reconstruction, while the magenta points are based on extracting δW from TRANSP runs. Shot numbers are indicated for certain discharges discussed in this report.

- The χ^2 measure of goodness of fit from axisymmetric equilibrium codes such as EFIT or LRDFIT is not higher in EP H-mode than standard H-mode.
- The apparent shift between the T_e and T_i pedestals is present for cases where the local velocity minimum goes to zero, or is finite at a few kHz
- The relative position of the T_e and T_i pedestals is the same for both polarities of the OH current and for various phases of the n=3 applied field. The error field due to the OHxTF interaction was the dominant n=1 error field in NSTX [45], and changed sign as the OH current changed sign. Hence, one might expect the toroidal phase of the apparent 3D distortion to shift with the shift of the applied field. Alternatively, if the 3D disruptions manifest themselves at higher toroidal mode number, then they might change phase with the n=3 field phase.

Hence, the present study will use purely axisymmetric analysis techniques, while acknowledging that this may obscure some important 3D effects.

With regard to rotation profiles, it should be noted that the profiles in Fig. 5.5b) or Fig. 5.7d) are among the most broad in observed in NSTX, a feature which is quite stabilizing to low-n global MHD. This may help explain why discharge 134991 sustains β_N>6, albeit with some degree of global activity, while discharge 141133 is nearly quiescent at β_N~5. On the other hand, the profiles in Fig 5.8 would be less desirable from the global stability perspective, as they are too peaked. The favorable profiles, which tend to manifest themselves in the later-transition long-pulse EP H-mode examples, provide clear motivation for pursuing the EP H-mode regime for next-step ST development. However, the examples also show that it is necessary to learn how to optimize and control the EP H-mode profile shapes, in order to fully exploit the configuration.

2.1.4: Stored Energy Increments During EP H-mode

A large database of EP H-mode discharges has been compiled; the results of this database are included in the figures in Sect. 1 of this report. That database assembles quantities measured just before the H-mode to EP H-mode transition, and then at a time when the EP H-mode has fully developed. The database uses quantities from both TRANSP [46] and the equilibrium codes EFIT [47-49] and LRDFIT [50]. The database also includes pedestal parameters extracted from the tanh fits to the edge profiles, using the functional form described in Section 2.1.3. Both the NSTX Thomson Scattering [51] and toroidal CHERS diagnostics [52] are oriented horizontally at the vessel midplane, allowing measurements of quantities with respect to the outboard major radius without any additional mapping step. Hence, the tanh fits utilized here are typically constructed as a function of major radius.

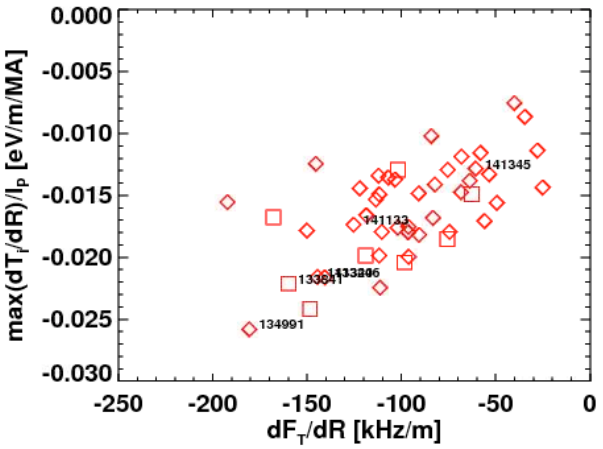

Fig. 5.10: The maximum ion temperature gradient, normalized to the plasma current. Diamonds are for EP H-mode configurations as in Fig. 5.5a) and b), and squares are for configurations as Fig. 5.5c)

The figures above show that there is a substantial increase in the stored energy following the EP H-mode transition. An important question to assess is which kinetic species was responsible for this energy increment. Fig. 5.9 shows the electron and deuterium energy increments as a function of the total energy increment. The electron and deuterium energy increments are determined from

integrating the thermal pressure of those species using TRANSP. The total energy increment is determined from either MHD equilibrium reconstruction (orange) or from the total thermal energy increment computed by TRANSP. This figure shows clearly that the primary increment of energy occurs in the ion channel, with ~75% of the energy increase appearing in the deuterium. Approximately 25% of the energy increase is typically found in the electrons, with negligible increases in the impurity and fast ion energy. Note that these ratios are typical of both cases with the T_i steep-gradient region shifted inward from the separatrix (squares), and cases where it is located nearer or at the edge (diamonds).

2.1.5: Relationship between Rotation and Ion Temperature Gradients

Previous analysis of a small set of EP H-mode cases indicated that the ion temperature pedestal height scaled roughly with toroidal rotation shear at that same location. As part of the present research, this relationship was examined for a larger number of examples. The results of this study are shown in Fig. 5.10.

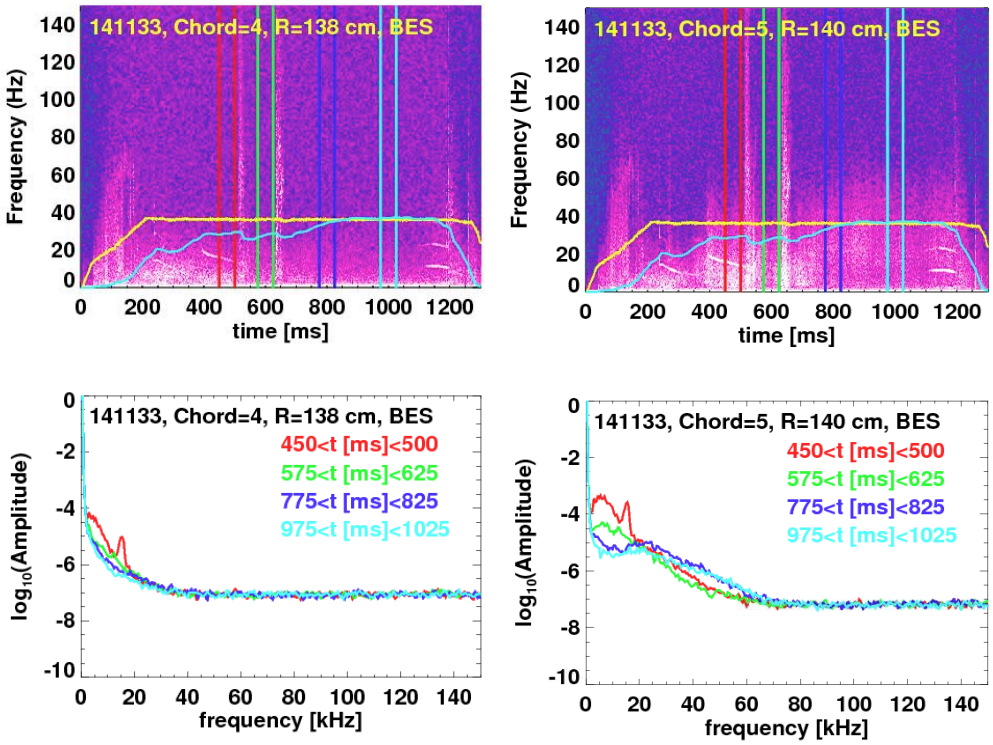

Fig. 5.11: BES fluctuation spectrum data for long-pulse EP H-mode discharge 141133. The upper frame shows the spectrogram, along with the plasma current in yellow and the normalized β in cyan. The lower frames show the average spectrum computed during the time between the vertical lines in the upper frame. The measurement locations of R=1.38 and 1.4 m are in the steep gradient region (see Fig. 5.7).

While the previous analysis used the pedestal height as a figure of merit, that proved problematic for the present case due to the inclusion of discharges such as in the right column of Fig. 5.5. These cases have a substantial "vertical" offset to the T_i profile due to the region with smaller gradient outside of the steep gradient region. Hence, for this analysis, the maximum value of dT_i/dR is used to parameterize the strength of the EP H-mode. Furthermore, it was found that the trends in the data were more clear if the gradient were scaled by the equilibrium plasma current. The x-axis in this plot shows the rotation gradient in the region inside of the local rotation minima. It is clear that, within the not insignificant scatter, the confinement as captured by this measure of the ion temperature gradient does indeed scale with the local rotation shear, for cases with the T_i gradient both near and farther from the separatrix.

2.2 Observation of Edge Fluctuations in EP H-Mode

A dedicated effort has gone into examining the edge turbulence during the EP H-mode phase of these discharges. Fluctuations under consideration have included magnetic fluctuations as assessed by edge Mirnov coils and density fluctuations as assessed by both the FIReTIP interferometer and the Beam Emission Spectroscopy (BES) system [53,54].

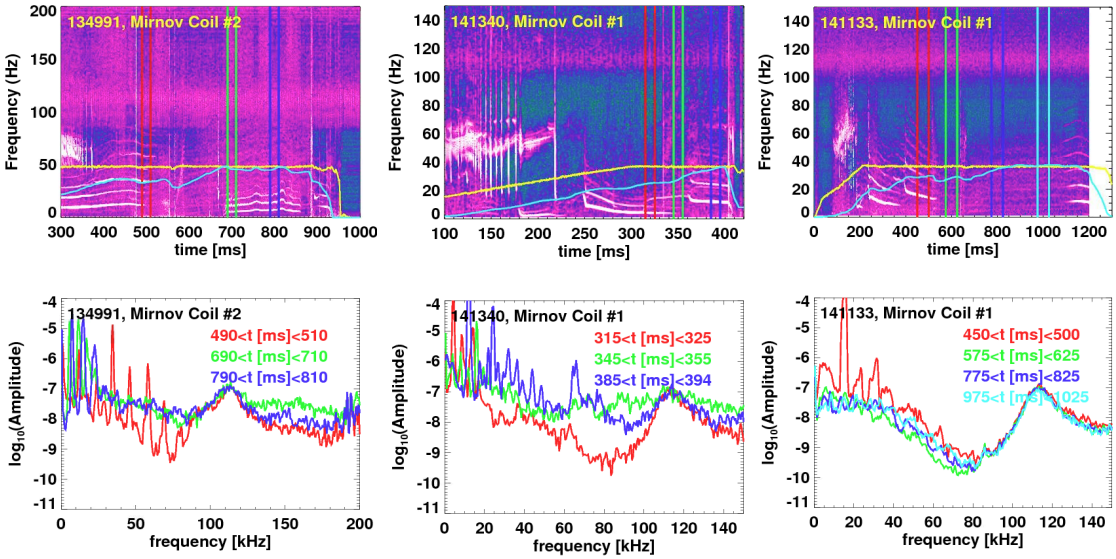

Fig. 5.12: Spectrograms of edge magnetic fluctuations in three EP H-mode examples. The EP H-mode phases are indicated in green and blue on the left, green and blue in the center, and blue and cyan on the right.

Example fluctuation data from the BES diagnostic is shown in Fig 5.11, for the long pulse EP H-mode case 141133. The top frame shows a spectrogram of the data, while the frame shows four spectra; the times used in computing the four spectra are bound by the vertical lines in the upper frame. The radii of the measurements, R= 1.38 &

1.40 m, are directly in the pedestal region of interest, as can be seen in Fig. 5.7. The first two time slices (red and green curves) correspond to the H-mode phase of these discharges. These are generally featureless, except for a 15 kHz mode in the earlier frame (these modes are common in the early phases of NSTX discharges [55]). The two later times are during the initial and later EP H-mode phase of this discharge. Interestingly, there is no observable reduction in the measured turbulence during this phase. Indeed, if anything, there may be a small increase in the fluctuation amplitude during the EP H-mode phase (though this may also be due to the larger density during this later phase). This result is generally typical of the BES measurements during EP H-mode, where clear reductions in turbulent amplitude have been difficult to identify. Similar results were found when examining the line-averaged density fluctuation amplitudes from the FIReTIP diagnostic.

While the results of the BES and FIReTIP fluctuation analysis were disappointing, there may be signatures of the relevant physics in the edge magnetics signals, as analyzed in Fig. 5.12. The left and center columns correspond the discharges illustrated in Fig. 5.5. In both these two cases, there are clear increases in the level of magnetic fluctuations between 50 and 100 kHz during the EP H-mode phase, compared to the proceeding H-mode phase. For 134991 (left column, long-pulse, high-β example), there are a series of low-frequency modes, which have been identified as n=2-4 modes from phase analysis. These fluctuations are not by any means ubiquitous to EP H-mode plasmas, and the more significant effect may be the broadband fluctuation increase. Discharge 141340 (center column, early EP H-mode transition example from Fig. 5.6) shows the standard low-f mode activity that occurs as the current profile evolved in NSTX [55]. However, the increased magnetic fluctuation amplitudes are also observable following the EP H-mode transition at t=0.33 s.

However, while these magnetic fluctuation observations are encouraging, is must be noted that these observations are not ubiquitous . For instance, discharge 141133 (left column, quiescent long-pulse EP H-mode example), does not show any particular increase in magnetic fluctuation amplitude. Hence, while these magnetic fluctuations may play some role in the EP H-mode physics, other elements must be at play as well.

2.3 Calculations of turbulence and transport in EP H-mode Mode plasmas

2.3.1: Assessment of thermal transport with XGC-0

XGC0 [56] is a code that leverages high-performance computing to calculate the self-consistent full-f drift-kinetic solution for ion transport in the H-mode pedestal using a realistic diverted magnetic geometry and Monte Carlo neutral recycling model. The large computational resources required to solve the full-f solution is justified on the observation that kinetic ion effects (such as ion orbit loss and finite orbit effects) have significant impacts on the ion thermal, particle and momentum transport in the H-mode pedestal and scrape-off layer.

The code was recently updated to enable quantitative comparison to experimental measurements in order to quantify the role of axisymmetric neoclassical transport in various H-mode transport regimes. These updates include: (1) addition of impurity ions to the simulation since most ion diagnostics measure the properties of plasma impurities, (2) synthetic diagnostics for typical profile diagnostics on NSTX and DIII-D, such as charge-exchange spectroscopy and Thomson scattering, and (3) improved code diagnostics that track the contributions of different transport processes on the energy, particle and momentum balance.

The ability to quantitatively compare the simulation to experimental measurements has enabled XGC0 to be used as an interpretative transport model. Ad-hoc anomalous transport is added to the neoclassical transport level if it is needed to improve the agreement between the simulation and experimental measurements.

Interpretative XGC0 was used to investigate the neoclassical ion transport in an EP H-mode discharge with transport approaching saturation (discharge 141133, discussed in Fig 9.7, at 900ms).

The neoclassical thermal transport calculated by XGC0 is found to reasonably reproduce the levels seen in experiment throughout the simulated pedestal and SOL domain ($0.6 < \psi_N < 1.1$). However, the neoclassical momentum transport rate inside of $\psi_N < 0.9$ is under-predicted. The requirement of anomalous momentum transport may be an indication that non-ambipolar electron transport (such as fluctuation-induced Reynolds and Maxwell stress) is a significant source of momentum transport in NSTX.

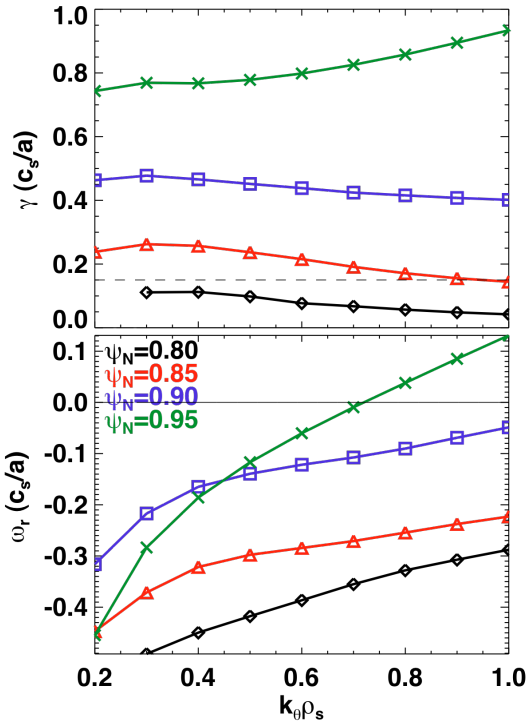

Fig. 5.13: Spectra of the growth rate (top) and real frequency for TEM-like modes in the EP H-mode pedestal. The different colors correspond to different radial locations.

The simulation also indicated that the neoclassical particle transport was sufficient to reproduce the experimentally measured density profiles with realistic neutral-beam and recycling particle sources. However, this result was achieved using an enhanced electron mass that was 1% of deuterium (as opposed to 0.028%), so the dependence of the simulated neoclassical particle transport on the mass of the electron needs further investigation.

The XGC0 simulation results suggest that EP H-mode achieves a level of ion thermal and particle transport that approaches the

neoclassical limit throughout the pedestal and SOL. However, the ion neoclassical transport is influenced by the details of the turbulent electron transport through collisional coupling and anomalous momentum transport. Thus, the transition from H-mode to EP H-mode may represent a bifurcation in the electron transport that self-consistently modifies the ion neoclassical transport. This hypothesis will be investigated in the future by comparing the neoclassical ion transport in EP H-mode conditions to standard H-mode scenarios on NSTX using interpretative XGC0 analysis.

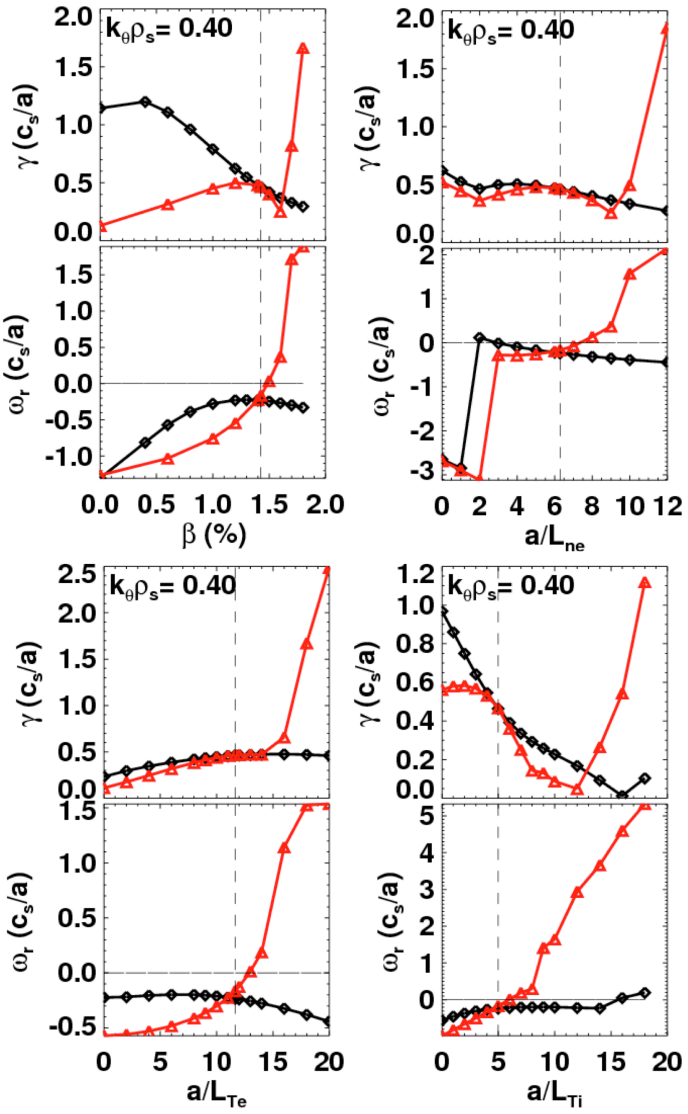

Fig. 5.14: Growth rate and real frequency of the dominant instabilities in the example EP H pedestal, as a function of upper left) β, upper right) the density gradient, lower left) the electron temperature gradient, and lower right) the ion temperature gradient

2.3.2: Assessment of microstability with GS2

The gyrokinetic stability of an EP H-mode discharge is being analyzed using the GS2 code [57]. Kinetically constrained MHD equilibria are used in these calculations, along with the fitted edge profiles used to generate these reconstructions. Three kinetic species are included—deuterium and carbon ions along with electrons—and the simulations are fully electromagnetic and include pitch-angle scattering collisions. Initial efforts focused on grid resolution checks at several edge radii to ensure the solutions are converged. Spectra of the growth rate and real frequency are shown in Figure 5.13 for four edge radii roughly spanning the EP H-mode pedestal. The real frequency along with eigenfunction structure (not shown) indicate that TEM-like modes are dominant throughout the pedestal, with the exception of a mode propagating in the ion diamagnetic direction at higher k_y at the outermost radii. The growth rates increase with radius, and over much of the pedestal are

significantly larger than the ExB shear rate (indicated by the dashed horizontal line). At radii further in than shown here (ψ_N=0.7 and 0.75), modes in the wavenumber range considered are stable.

The scaling of the frequency with various parameters such as gradient scale lengths and β have been calculated for a radius of ψ_N=0.90 (roughly at the mid-pedestal). These scans have been performed two ways: 1) by varying gradient scale lengths only, while leaving the magnetic geometry fixed, and 2) by using a local MHD equilibrium model to change the pressure gradient within the magnetic geometry and keep it consistent with the (varying) parameters during scans. This is an important difference, since increasing the pressure gradient in the MHD equilibrium tends to be strongly stabilizing, and can partially or even fully offset the destabilizing effect of increasing (for example) the temperature gradient. In Fig. 5.14, results using the first method (single parameters varied individually) are shown as the red curves, while those using the second method (geometry recalculated using a pressure gradient consistent with the other parameters at each point in a scan) are shown in black.

As the figure shows, if the geometry is held fixed, increasing any one of β, the density gradient, or the electron and ion temperature gradients by less than a factor of two causes a kinetic ballooning mode to become destabilized (as evidenced by a sharp increase in the growth rate and a strongly positive real frequency). However, with a consistent MHD equilibrium calculated at each point, KBM onset is never observed. This is consistent with the plasma being in the second-stable regime, which has been verified through calculations of ideal ballooning stability. At the nominal parameters (vertical dashed line), increasing the electron temperature gradient has the strongest destabilizing effect. The density gradient is weakly stabilizing, with microtearing modes appearing at very low values of a/L_{ne} (evidenced by the transition to large magnitude negative real frequency). Increasing the ion temperature gradient is strongly stabilizing, regardless of how the geometry is treated (aside from the transition to KBM). This suggests that the increased ion temperature gradient measured in the EP H-mode does not lead to degraded microstability, and may be consistent with the dominance of neoclassical transport in the ion channel. Overall, the dependencies found here are reasonably consistent with the dominant mode being a TEM/KBM hybrid mode as found in pedestal calculations during standard and lithiated H-modes [58], with a smooth transition between negative and positive real frequency as the KBM threshold is approached (in the case where the geometry is held fixed). One difference, however, is the β dependence found here, where increasing β is stabilizing near the nominal value even in the case where the geometry is not changed.

2.3 Prospects for EP H-mode Utilization in NSTX-U and next step STs.

One criterion for extrapolating the EP H-mode for next-step devices is the demonstration of quasi-stationary conditions for many energy confinement times. This has been shown in Fig. 5.3. A second criterion is to establish a mechanism to trigger and control the transition to this regime.

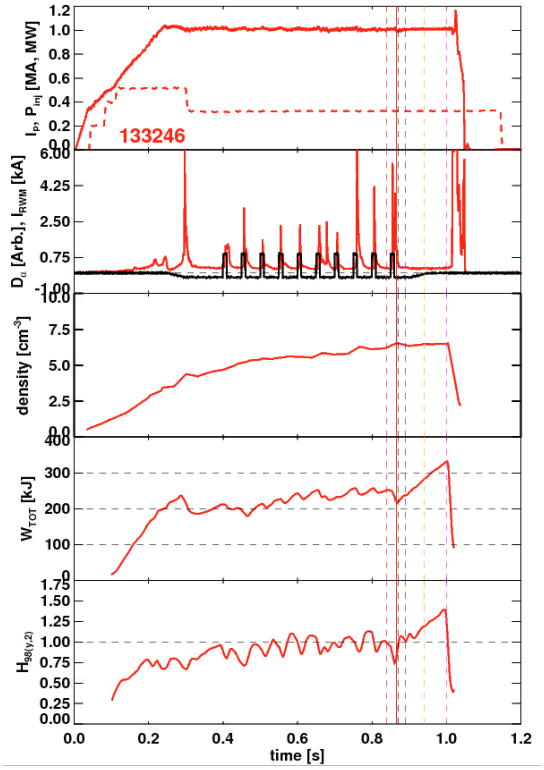

Fig. 5.15: Example of EP H-mode configuration initiated by a triggered ELM. Shown are the plasma current and injected power, D_a and RWM coil current, line-averaged density, stored energy, and $H_{98(y,2)}$ confinement multiplier. The dashed vertical lines indicated the times of the profiles in Fig. 5.16.

density ramp is largely arrested, at least for the duration of this EP H-mode example, while the stored energy and confinement increase compared to the H-mode phase. Note that there are other examples of the externally triggered EP H-mode transitions, all of which come from the RWM ELM triggering experiments.

Given that a spontaneous ELM is often observed to trigger this regime, it seems reasonable to examine whether an externally triggered ELM can have a similar effect. As shown in Fig. 5.15, this is indeed the case. The top frame shows the plasma current (I_P=1 MA in flat-top) and beam power for this discharge. The second frame shows the current in a representative RWM coil in black and a D_α trace in red. It can be seen that there are small transients in the current, and that these trigger ELMs [42-44]. The RWM coil configuration in this case is configured to produce pulsed n=3 fields, which have shown to trigger ELMs over a range of conditions. In the present case, the transition to the EP H-mode configuration follows the final triggered ELM. The following frames show the line-averaged density, stored energy, and $H_{98(y,2)}$ confinement multiplier. In this case the

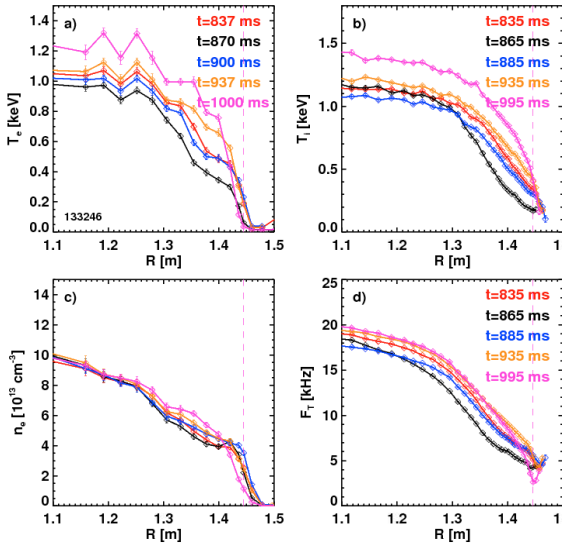

Fig. 5.16: Profile evolution following the ELM-triggered EP H-mode in Fig. 5.15

Fig. 5.16 shows the profiles before and during the EP H-mode phase of the discharge; the chosen colors match the vertical lines in Fig. 5.15, indicating the relative timing between the frames. The behavior for this externally triggered EP H-mode is similar to that in previous cases, with the ELM at t=0.865 s leading to a significant drop in both the edge ion temperature and rotation. The local minima in the rotation profile can be found for

some time slices in the following EP H-mode phase. The region of steep T_i gradient is localized to the very edge of the CHERS measurement, and the rotation profile takes on broad structure. Hence, this triggered EP H-mode case shows all the features of the most attractive previously illustrated spontaneous transition examples.

Beyond initiating the EP H-mode configuration with triggered ELMs, it remains possible that specialized 3D fields at the plasma edge could trigger this configuration. It appears that the field configuration most likely to trigger these configurations will have fairly high-n, in order to minimize the core perturbation. It is conceivable that either resonant fields, which may lead to island opening, or non-resonant fields, which would brake the plasma rotation via the NTV effect, may be optimal for setting up the rotation profile required for the EP H-mode configuration. These options will be explored with the NCC coil in NSTX-U.

2.4 Future Research Directions for Enhanced Pedestal H-mode Research.

The research described above indicates key future directions for EP H-mode research. With regard to profile analysis, the poloidal flow should be included in the radial force balance analysis. This flow was not routinely measured in NSTX, and it may be that TRANSP/NCLASS calculations of the anticipated impurity flow will be necessary to compute the $V_\theta B_T$ term.

The XGC0 analysis will also warrant further work. Now that creditable calculations for this EP H-mode example have been completed, it will be valuable to compare them to standard H-mode case. This work is ongoing.

Experimentally, reliable access to the EP H-mode configuration is an important consideration. Once experiments are initiated on NSTX-U, triggering methods for the EP H-mode configuration will be revisited. These will include further efforts to sustain the naturally occurring EP H-mode configurations that often occur early in the discharge in high current cases, or to trigger EP H-mode configurations at lower q_{95}.

3.0 Physical Mechanisms Behind Transport in the ELM-Free H-mode Pedestal

Experiments in NSTX have shown that with the application of lithium conditioning to the PFC, ELMs are eliminated [34] and confinement improves [39,59]. While these are nominally positive changes, strong accumulation of impurities has been observed in these discharges [60], a characteristic that must be eliminated in order to achieve a stationary condition. In this section, recent research on the transport dynamics of these ELM-free H-modes is presented. The transport of lithium and carbon, including detailed comparisons to neoclassical theory, are presented in Section 3.1; note that some aspect of this study were reported in the FY-12 JRT report, but are repeated here due to their timeliness and relevance. New studies of pedestal microstability are presented in Section 3.2.

3.1: Assessing Impurity Transport in ELM-Free H-Mode

As has been documented in numerous publications and is noted in the introduction, lithium-conditioned discharges in NSTX have excellent confinement [59,60], few or no ELMs [34,61], well-controlled deuterium inventories [35], low levels of lithium contamination [62], and high levels of carbon accumulation [60]. This high level of carbon accumulation prevents these regimes from reaching stationary conditions, providing a significant barrier to extrapolating them to next-step STs.

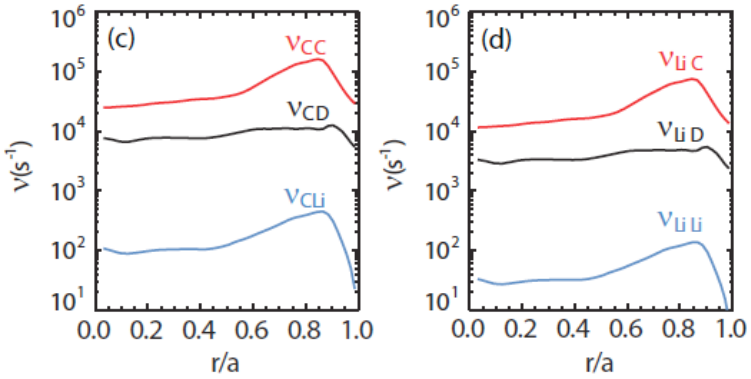

Fig. 5.17: Test particle collision frequencies for carbon (left) and lithium (right).

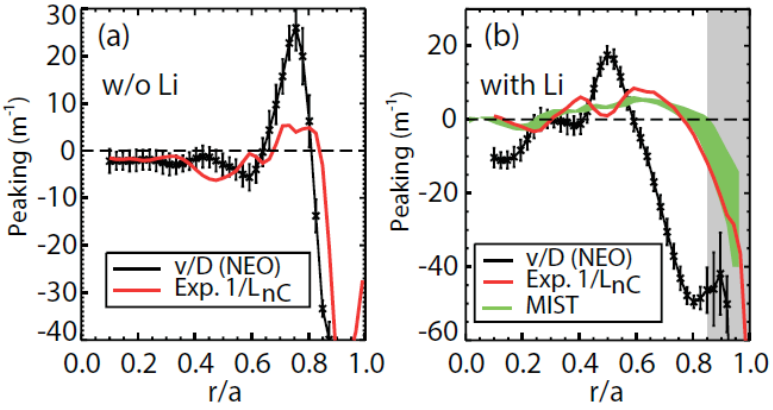

Fig. 5.18: Comparison of the experimental and neoclassically predicted peaking factors for carbon for a case without lithium PFC conditioning (left) and with lithium PFC conditioning (right)

Recent research has provided significant insight into the dynamics of lithium and carbon transport in these regimes [35,63.]. This research uses carbon and lithium profiles [67] from the CHERS diagnostics, and electron density and temperature data from Thomson scattering. The neoclassical transport of carbon and lithium is assessed with the NEO [64] and NCLASS [65] codes, which compute both a diffusivity D and a convective velocity υ. The MIST code was used, in either interpretative or fully predictive mode, to solve the impurity transport equations. Key results from that research are summarized here.

To develop some initial intuition about the dominant neoclassical impurity transport mechanisms, the various relevant collision frequencies were studied. As indicated in the left frame of Fig. 5.17, carbon collisions with background deuterium ions dominate the carbon transport (like-particle collisions do not generate particle transport). Indeed, a factor of 100 increase in the measured lithium concentrations would be required to meaningfully change the calculated carbon transport coefficients. Hence, modifications to

the neoclassical carbon transport due to lithium PFC conditioning must be due to changes in the background deuterium parameters. The lithium neoclassical transport, on the other hand, is dominated by collisions with carbon impurities.

A first part of this study addressed carbon transport in discharges with and without lithium conditioning; the case without lithium PFC conditioning had medium sized type-I ELMs. The results from this study are summarized in Fig. 5.18, where profiles of the peaking factors are plotted. The experimental peaking factor of the profile quantity f(r) is denoted by $1/L_f = \frac{d}{dr}\ln(f)$, based on measured profiles. The predicted neoclassical peaking is, for a source free region, given by the ratio υ/D, where these quantities are both computed with NEO in the present example. Here, υ is the inward convective (pinch) velocity, while D is the diffusion coefficient.

For the case without lithium conditioning on the left, the predicted peaking agrees will with neoclassical predictions in the core (r/a<0.6) and in the edge (r/a>0.8). A significant discrepancy exists in the vicinity or 0.6<r/a<0.8, with the neoclassically predicted peaking being quite high. This local maxima is not found in the experimental results. This difference is likely due to the flushing of impurities in this radial region due to ELMs, an effect not captured in the present modeling.

For the lithium conditioned case, qualitative agreement is found between the neoclassical modeling and experimental result, including an outward convection region for 0.2<r/a<0.6 and an strong inward edge pinch. However, discrepancies exist in the core, and more importantly the pedestal top region of r/a~0.6-0.8. The different signs in this region suggest either an anomalous convective contribution or a deficiency in the neoclassical model. This is confirmed by the semi-predictive MIST runs illustrated in green in the right-hand frame. Here, the diffusivity was set at the neoclassical value, but the profile of the convective term was adjusted to give agreement with the measured values. One explanation for this anomalous behavior may be ion scale microturbulence. This would be in line with the observation of ion thermal transport in excess

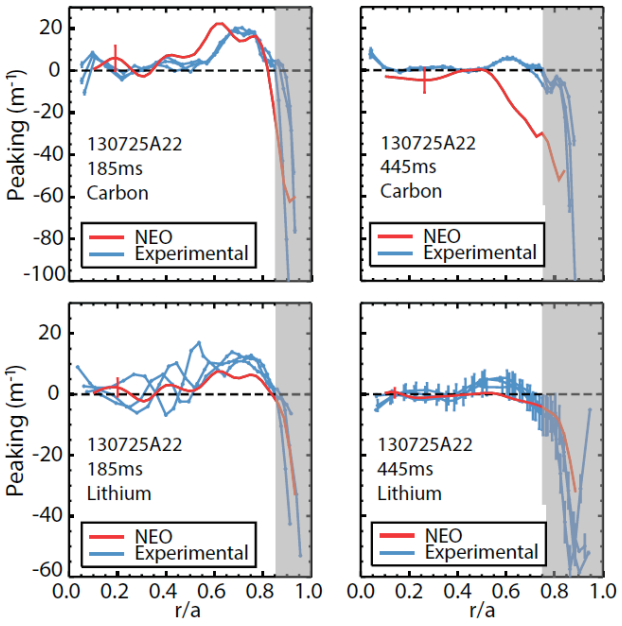

Fig 5.19: Peaking factors for carbon (top) and lithium (bottom) for time early (left) and late (right) in the discharge.

of the neoclassical level is recent low-collisionality lithium conditioned discharges. Alternative explanations include a breakdown in neoclassical theory for large values of ρ_{pol}/L, or uncertainties in the deuterium density profile resulting in errors in the derived impurity transport coefficients.

Fully predictive MIST simulations of these discharges with neoclassical transport coefficients indicated that the profile changes with lithium conditioning do not alone account for the increase in carbon concentration; the lack of ELMs clearly plays a significant role. However, the change in neoclassical transport coefficient leads to a deeper penetration of impurities to the core, where they would be less sensitive to flushing by ELMs. This may explain the observation that even when ELMs were triggered by 3D fields in otherwise ELM-free lithium-conditioned discharges, the core impurity accumulation remained a problem [42-44].

These studies also assessed whether lithium transport showed anomalies similar to that for carbon. Neoclassical calculations with NCLASS and NEO shows that the lithium diffusivity is ~10 times larger than that of carbon, with convective velocities within a factor of 2 of the carbon values across the full profile. These calculations, along with the experimental profiles, allow a comparison of peaking factors in Fig. 5.19. The left side of that figure shows that early in the discharge, the experimental and theoretical peaking factors are in good agreement. At later times, a significant deviation in peaking for carbon is observed. This is similar to that discussed in reference to Fig. 5.18, illustrating the generality of that result. However, the measured lithium peaking follows the neoclassical calculation quite well.

Finally, this research examined the question of whether neoclassical physics alone could explain the significant difference in core concentrations between lithium and carbon $\left(N_{Li}/N_C < 0.01\right)$. The experimental carbon profiles show a decrease of ~100 from r/a=0.8 to r/a=1.0, while lithium density profiles show a smaller decay of a factor of 10. Hence, in appears that differences in the radial transport can only explain up to a factor of 10 in the n_{Li}/n_C ratio, and that differences in the sources profiles and SOL parallel transport likely play a significant roll as well. Considering neoclassical transport only, the density at r/a=0.8, normalized to that at the edge, can be given by $\exp\left(\int_{r/a=1.0}^{r/a=0.8}\left(v/D\right)_{neo}dr\right)$. By this line of argument, the normalized carbon densities at r/a=0.8 are projected to be between 10 and 1000 times higher than the lithium densities. Hence, neoclassical transport can explain the differences in the impurity concentrations, though the effect is reduced by the apparent non-classical behavior of carbon and differences in the edge sources.

Interested readers should examine Refs [35,63] for more information on these topics, including measurements and modeling of impurity generation and SOL transport.

3.2: Assessing Turbulence in NSTX Lithiated ELM-Free H-modes

The NSTX Beam Emission Spectroscopy (BES) diagnostic [53,54] was designed to study low-k pedestal and core turbulence in a variety of operating modes. In recent analysis, the parametric scaling of both poloidal correlation lengths [66] and turbulent amplitudes [36] with plasma parameters have been studied, and comparisons to gyrokinetic stability calculations have been made [36]. This section summarizes the very recent results on the pedestal turbulent amplitude analysis and stability calculations [36], in order to better understand the transport processes in the high-performance ELM-free pedestal plasma.

The analysis here is taken from>200 ms long windows during ELM-free, MHD quiescent periods of discharges with 700 <I_P [kA]<900 and B_T=0.45 T. All of these discharges had lithium conditioning of the plasma facing components. A total of 129 such data windows are used in the present analysis. The BES signals have been filtered to isolate the 8-50 kHz features. They are used to measure the normalized plasma density fluctuations as $\frac{\tilde{n}}{\langle n \rangle_{DC}} = C \frac{\tilde{I}_{D\alpha}}{\langle I_{D\alpha} \rangle_{DC}}$, where $I_{D\alpha}$ is the measured BES intensity and C=C(E_{NB}, n_e,T_e,Z_{eff}) is given by 2.24. Kinetic profile parameters such as ∇n_e or T_i are inferred from Thomson scattering and CHERS, while equilibrium parameters such as β_P or $\hat{s}$ (magnetic shear) are derived from EFIT reconstructions.

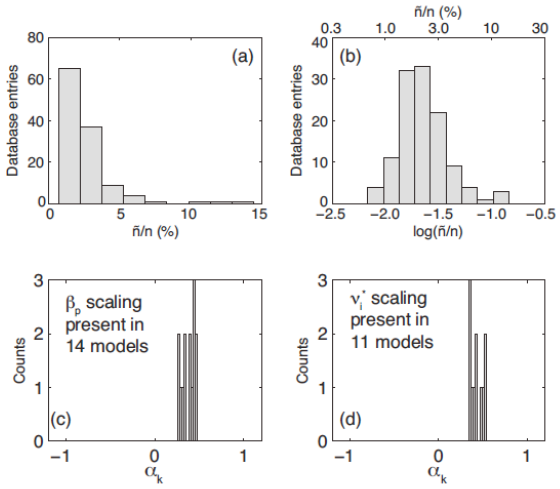

Fig 5.20: distribution of a) δn/n and b) log(δn/n). Also shows are the scalings that emerge from model aggregation for the β_P and ν_i dependence of log(δn/n).*

The analysis of this data is done using stepwise multivariate linear regression (SMLR) and model aggregation. Taking y_i as denoting a turbulence characteristic and $x_{k,i}$ as a plasma parameter, the SMLR algorithm finds models in the form

$$\frac{\hat{y}_i - \bar{y}}{\sigma_y} = \sum_k \alpha_k \frac{x_{k,i} - \bar{x}_k}{\sigma_k}.$$

Here, σ are standard deviations, $\hat{y}_i$ are model parameters for turbulence quantities, and the dimensionless α_k parameters are linear scaling coefficients between y_i and $x_{k,i}$ (i indexes database entries and k indexes plasma parameters). The SMLR algorithm minimizes the model's squared sum of errors, by adding or removing parameters x_k such that the inferred significance of each α_k value exceeds 95% [67]. Because many statistically valid models exist in the high-dimensional x_k space, a model aggregation technique is used. This provides i) more parametric scalings than a single model, and ii) a distribution of scaling coefficients that cover a variety of model constraints. More details on the SMLR process as applied to NSTX data can be found in Refs. [66] and [36].

Some inputs and outputs from this process are shown in Fig. 5.20. The top row shows the distribution of $\tilde{n}/n$ and $\log(\tilde{n}/n)$ for the present database. The highly skewed distribution of $\tilde{n}/n$ proved problematic for the SMLR analysis, while fits to $\log(\tilde{n}/n)$ worked well and are used for the analysis below. The bottom two rows show the range of scaling coefficients for β_P and ν_i* from model aggregation. The positive coefficients imply that $\log(\tilde{n}/n)$ does indeed increase with these two parameters.

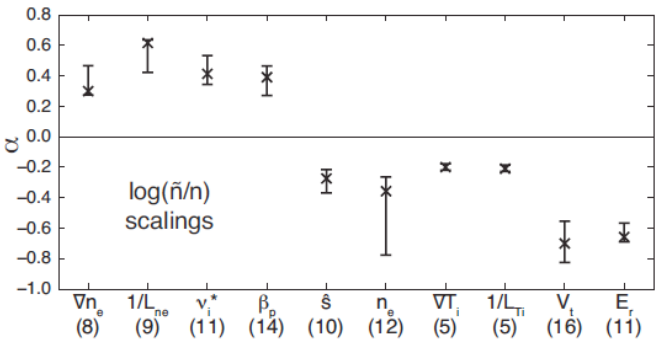

Fig 5.21: 10th to 90th percentile ranges for scalings derived from model aggregation for log(δn/n). α>0 denotes a positive scaling, and the number below each label indicated the number of models that contain the scaling.

A larger set of scaling parameters is shown in Fig. 5.21. Positive scaling of $\log(\tilde{n}/n)$ is observed for ∇n_e, $1/L_{ne}$, ν_i* and β_P. On the other hand, negative scalings were observed with $\hat{s}$, n_e, ∇T_i, $1/L_{Ti}$, V_t, and E_r. The positive scalings with ∇n_e and $1/L_{ne}$ indicate an instability driven by the density gradient, such as the Trapped Electron Mode (TEM) or Kinetic Ballooning Mode (KBM) instability. However, the positive scalings for the density gradient and negative scalings with the ion temperature gradients are notably inconsistent with ion temperature gradient (ITG) driven turbulence; this conclusion is similar to that drawn from the analysis of poloidal correlation lengths using BES [Smith 2012]. Positive scalings with collisionality are consistent with microtearing instabilities, but not drift-wave like turbulence such as ITG or TEM.

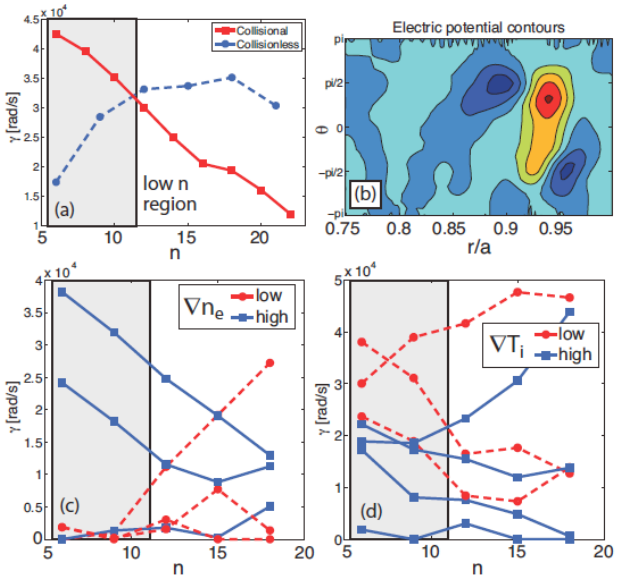

Fig. 5.22: a) simulated growth rates for collisional and collisionless cases as a function of n, b) field aligned electric potential contours. Growth rates then are shown for c) several high and low ∇n_e scenarios, and d) several high and low ∇T_i scenarios. The relevant low-n region is shown on the left in grey in frames a), c) and d).

These experimental results have been compared to results of linear stability calculations with the GEM code [68,69]. These calculations are electromagnetic, collisional, and global in the pedestal, using realistic profiles in the region of interest (0.75<r/a<0.99). They compute the linear stability of modes with 6<n<18 (the n=6-10

modes correspond to $k_\theta \rho_i \sim 0.2$, as typically observed in NSTX).

The results of these calculations are shown in Fig. 5.22. The collisionless and collisional calculations in frame a) show the collisional destabilization of low-n modes, or alternatively, that collisions shift the unstable mode to lower n; this is consistent with the observed positive scaling of $\log(\tilde{n}/n)$ with ν_i* in Figs. 5.20 and 5.21. Fig. 5.22b) shows the field aligned electric field contours, showing a mixed-parity structure (neither pure ballooning nor tearing parity) of the modes. Fig. 5.22c) shows growth rates from several high and low ∇n_e scenarios. These generally show higher low-n growth rates with high ∇n_e consistent with the positive ∇n_e scaling for $\log(\tilde{n}/n)$ in Fig. 5.21. Similarly, frame d) shows that the low-n growth rates are generally higher for low ∇T_i, consistent with the consistent with the negative ∇T_i scaling for $\log(\tilde{n}/n)$ in Fig. 5.21. The consistency between the GEM calculated growth rate trends and the observed ∇n_e, ∇T_i, and ν_i* scalings are quite encouraging, though conclusive identification of turbulent modes active in the pedestal and robust validation of pedestal models requires further analysis.

Interested readers should examine Refs [36,66] for more information on these measurements and calculations, including discussion of the statistical conditioning of the database and of BOUT++ simulations.

4.0 Edge Harmonic Oscillation Observations

As described in detail in the DIII-D section of this report, the attractive QH-mode regime is facilitated by an "Edge Harmonic Oscillation", or EHO. This mode appears to replace ELMs in providing the required particle transport, allowing an ELM free regime with stationary density and impurity content. While QH-mode was first observed in lower density regimes with counter injection, recent research has increased both the density window and co-injection torque for QH operation.

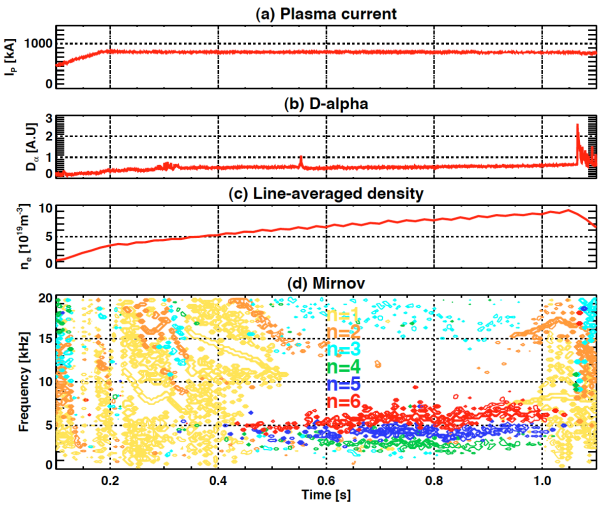

Fig. 5.23: Evolution of a discharge (138239) with observed low-n EHOs.

Motivated by these observations, an effort was made determine if such EHOs may exist in NSTX plasmas. This effort was successful in isolating EHOs, in both small-ELM regimes [70] and ELM-free, high-performance regimes with lithium conditioning [37,38] This report focuses on the latter regime. Unfortunately, the EHOs in NSTX were comparatively weak, and did not result in any observable contribution to the edge particle transport; the electron and carbon densities ramped in these discharges. Hence, the study here

will focus on aspects of the mode dynamics, and then on potential methods to drive the modes to larger amplitude in NSTX-U.

4.1: Observation of EHOs in NSTX Lithiated Discharges

4.1.1: Mode dynamics and structure

The general features of a discharge with EHOs are illustrated in Fig. 5.23 [37,38]. The upper frames show the plasma current, D_α emission from the lower divertor, and line average density. No ELMs are observed in this discharge, and, as noted above, the density increases throughout the discharge. The lower frame shows the spectrogram from wall-mounted Mirnov coils. The phase between 0.6 and 1.0 seconds is free of large amplitude n=1 and n=2 modes, which generally have a large impact on the plasma rotation and are often disruptive. However, a series of n=4-6 modes are clearly visible. These are the modes that are labeled as "EHOs" in the present research.

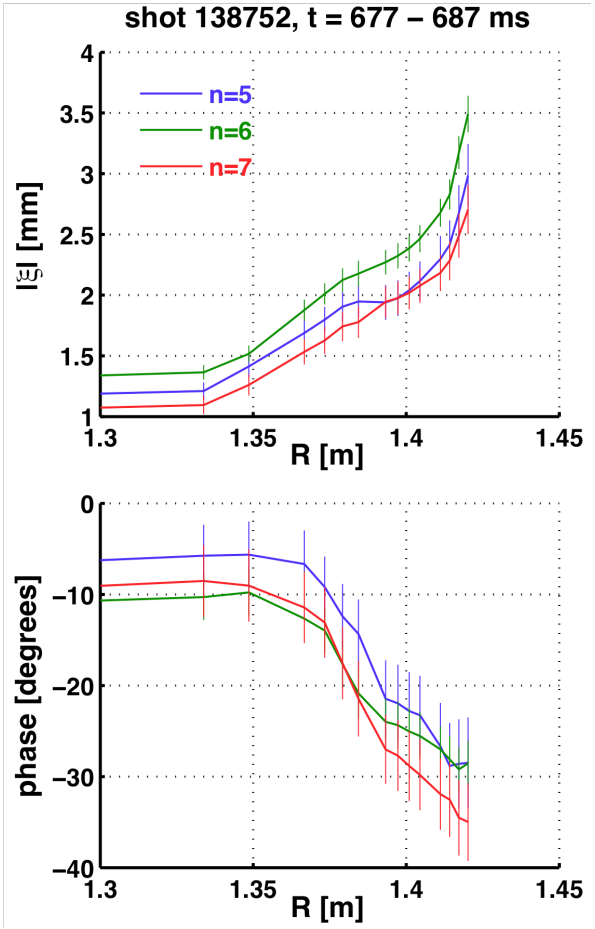

Fig. 5.24: Amplitude and phase of observed EHOs, as measured by the reflectometers. The separatrix is at 1.42 m in this discharge (138752).

These modes can be observed in the spectrograms of many other diagnostics, including edge soft X-rays when configured for low-energy emission measurements and Langmuir probes in the SOL near the outer strikepoint [37,38]. The low frequency of the modes, and their observation in diagnostics that are sensitive to the plasma edge, provides indication that the modes are indeed located in the vicinity of the separatrix.

In order to better assess the structure of these modes, their signature in the edge reflectometer [71] has been assessed. Fig. 5.24 shows the mode amplitude and phase for a discharge where the outer midplane separatrix is located at R=1.42 m. It is clear from the top frame that the mode displacements are in the range of 2-4 mm, and are peaked at the

plasma edge. The different mode harmonics are also highly coherent, as indicated by the bottom frame.

The edge-localized nature of these modes has been assessed via the NSTX BES [53,54] diagnostic as well; this data is available for a subset of the discharges where EHOs were previously identified. Figure 5.25 illustrates typical BES data for one of these modes. The top frame shows the radial profile of the density fluctuations, for peaks at ~3700 Hz and 5500 Hz. The primary fluctuation is localized to a just a few channels. The EFIT separatrix is shown as a dashed line, implying that the mode peak amplitude is at the separatrix. Note, however, that the separatrix location from these reconstructions is accurate to ~1 cm. Hence, the tanh fits to the density and temperature profile are also shown in the top frame. By comparing the fluctuation amplitude profile to the equilibrium profiles, it becomes clear that these modes are indeed located at the bottom of the pedestal, consistent with the reflectometer data. The lower frame of this figure shows the same fluctuation data, but with the fluctuation amplitudes normalized to the DC amplitude. This quantity is proportional to δn/n, and retains the strong peak at the bottom of the pedestal.

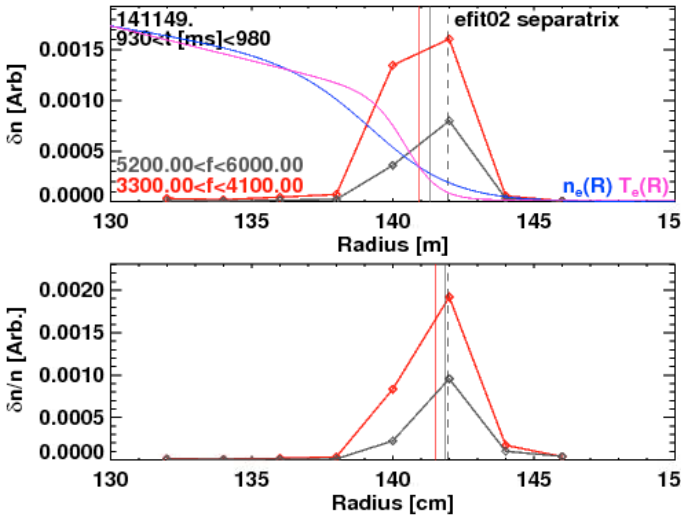

Fig. 5.25: Profiles of the BES fluctuation amplitude (proportional to δn_e) (top), and the amplitude normalized to the DC level (proportional to $\delta n_e/n_e$) (bottom). Both metrics show that the mode is localized to the plasma edge. The top frame additionally shows the tanh fit to the density and temperature profiles during this time period. The red curve is for an n=3 mode, while the black curve is for the n=4 EHO.

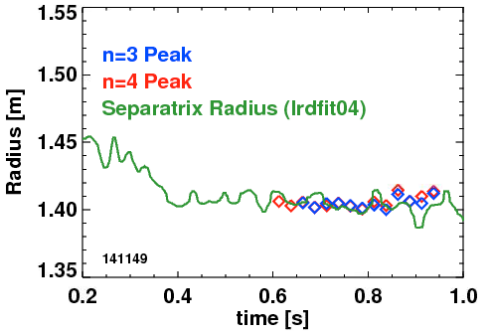

Fig. 5.26: Time evolution of the EHO peak amplitude radius and the separatrix radius.

The location of peak BES amplitude has been tracked, using the metric $R_{peak} = \sum R_i \frac{\delta I_i}{I_i} \Big/ \sum \frac{\delta I_i}{I_i}$. The result of such an exercise is shown in Fig. 5.26, which illustrates the positions of both the n=3 and 4 peak amplitudes as a function of time. As anticipated, they modes are located very near the separatrix for the duration of their existence.

4.1.2: Operational space for EHOs in NSTX

A Significant effort was dedicated to finding parameters where EHOs were possible in NSTX. However, clear trends were hard to find. Some observations include:

- Discharges with EHOs tended to have fairly large plasma wall gaps. No EHO discharge had an outboard plasma-wall gap less than 13 cm.
- Discharges with I_P=800kA were most likely to have EHOs. Higher plasma currents tended to eliminate EHO activity.
- There is some evidence that edge rotation shear in the range of -300 to -200 kHz/m may be favorable for EHO formation (see Figure 4 of Ref. [38]).

4.1.3: Peeling Ballooning Space

As part of the analysis of these cases, the peeling-ballooning stability [72] of these discharges was analyzed. This analysis used highly constrained kinetic EFITs as input to stability analysis with the MHD stability code ELITE [72]. In particular, once the equilibrium was reconstructed, variations in the edge pressure gradient (α) and current density were imposed to compute a family of nearby equilibria, with ELITE run for the full set of cases.

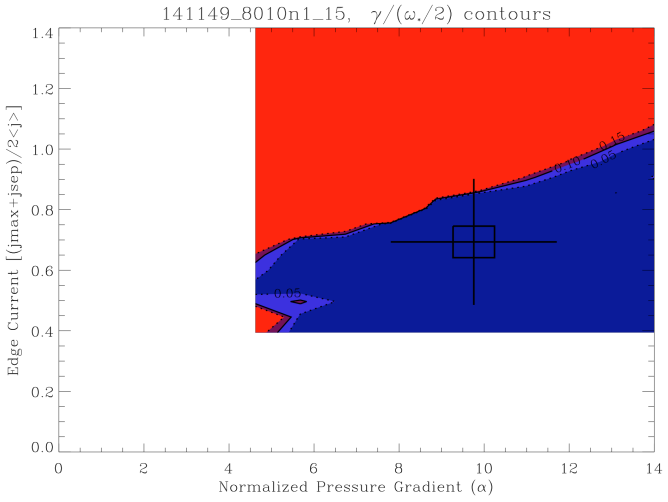

Fig. 5.27: ELITE calculation of the pedestal stability for a case with observed edge harmonic oscillations.

The results of this study are shown in Fig. 5.27, for the discharge 141149 discussed in Section 4.1.1. Blue indicates the stable region in this plot, while red indicates unstable configurations. The large cross indicates the experimental location of the discharge in this parameter space. The ballooning boundary, at large pressure gradient, is not visible in this diagram, as is often the case in NSTX [70] and other low aspect ratio configurations [73]. On the other hand, the peeling boundary, at large current density, is clearly visible. The experimental point resides near the peeling boundary. This is quite similar to the case of QH-mode in DIII-D, where the relaxed pedestal operating point is near the peeling boundary [74].

4.2: Prospects for Actively Driving EHOs in NSTX-U

It is conceivable that the lower collisionality pedestals of NSTX-U will result in stronger EHOs, potentially leading to a QH-mode like configuration. However, rather than rely on

this assumption, recent efforts have attempted to assess if EHOs can be actively driven [37,38].

The method assumed in this study relies on use of the 12-strap NSTX-U High Harmonic Fast Wave antenna, shown in the bottom left of Fig. 5.28. The recent upgrade to a center-grounded configuration allows the top and bottom of each strap to be independently fed. An example configuration for EHO studies is shown in the upper left of Fig 5.28, where six of the available 12 straps are used, with odd parity about both the midplane and a line separating groups of three straps. Other configurations of current polarities are of course possible, as will be described below. The right portion of Fig. 5.28 illustrates the 3D NSTX plasma cross-section, along with the RWM coils in red and blue and the model shapes for the HHFW antenna straps in black. Compared to the RWM coils, which are located outside the vacuum chamber, these straps are capable of producing higher toroidal mode number perturbations due to their smaller toroidal extent, and higher frequency perturbations due to their location inside the vacuum chamber. Engineering considerations related to powering the straps for this application, while important, are not considered in this report.

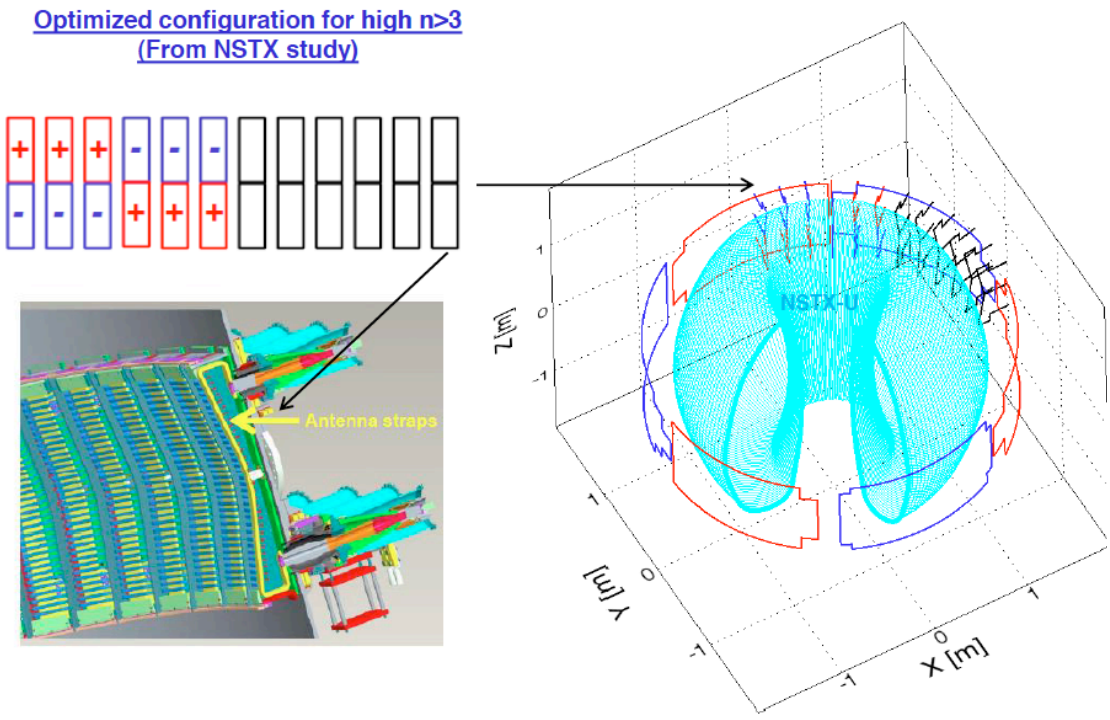

Fig. 5.28: NSTX-U antenna configuration for the driven EHO study. The upper left shows a schematic indication of the current polarities,, the lower left shows the mechanics of the current straps themselves, while the right figure shows the NSTX-U plasma boundary, the RWM coils (red and blue), and the modeled HHFW antennas (black).

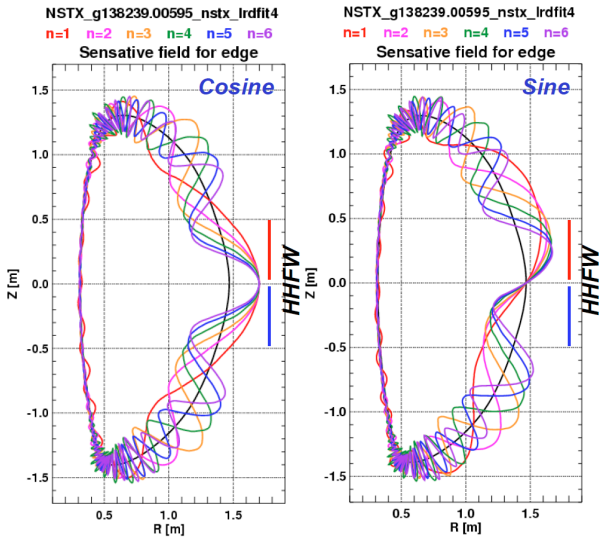

Fig 5.29: Dominant field component for n=1 to 6 perturbations, for a typical NSTX equilibria.

In order to assess the efficiency of driving edge perturbations with this antenna, the dominant external field for coupling to the plasma [75,76] is determined by the IPEC [77] code. This analysis essentially determines the configuration of the HHFW antenna currents that can most efficiently couple to the plasma and generate 3D distortions. As an example of this analysis, the dominant external field for each toroidal mode number n [37,38] is shown in Fig. 5.29. It is clear that the HHFW antenna will most easily couple to the sine part of the higher-n components, as its poloidal extent is comparable to the extent of the dominant field on the outboard side.

As part of an optimization study, 20-30 different combinations of antenna strap currents were tested for their coupling to the plasma via this overlap metric. The currents in each strap were always the same, and only the polarities varied. This constraint could be removed, through at the expense of more sophisticated power supplies. Fig. 5.30 shows in black the overlap field for the configuration that maximizes coupling to n=5 & 6 for the NSTX equilibrium (138239, q_{95}=9.3). Further, as shown in Ref. [37,38], the n≤3 part can be largely eliminated by the external RWM coils for low enough driving frequencies.

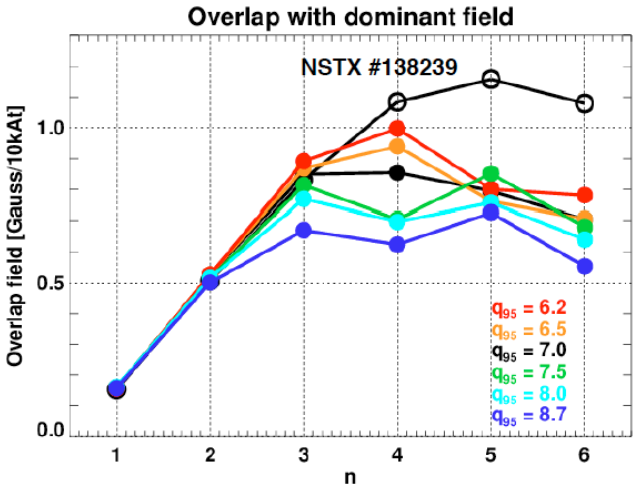

Fig. 5.30: Overlap of the applied field with the dominant field component as a function of toroidal mode number, for an NSTX-U q_{95} scan using model equilibria. The results for an NSTX case are also illustrated as the topmost black curve.

Fig. 5.31 connects the IPEC calculations back to the reflectometry measurements. The black points are the displacements for the n=6 reflectometry data, shown above in Fig. 5.24. The black lines show the displacement profile for 1 kA of current in

the HHFW antenna straps. It is clear that currents at that level, which are comparable to both the RF currents and the currents driven in the RWM coils, could produce displacements comparable to those naturally occurring. Hence, for somewhat larger currents, it may be possible to drive the modes beyond their present amplitude, potentially leading to beneficial changes in the edge plasma.

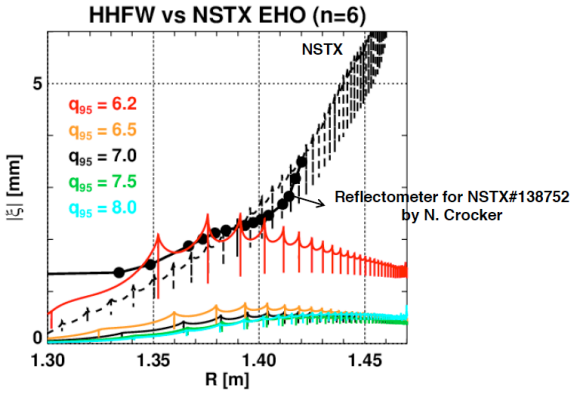

Fig 5.31: Measured displacements from reflectometery, overlaid on potential displacements for a single NSTX equilibrium and the NSTX-U q_{95} scan.

As a complement to the research presented in Ref. [37,38], these IPEC calculations were repeated for typical NSTX-U equilibria, over a range of q_{95}. The boundary shapes for these equilibria are shown in Fig. 5.32; these are high elongation and high triangularity equilibria of the type predicted to maximize the non-inductive fraction in NSTX-U [78]. β_N was fixed at 4.0 for all cases.

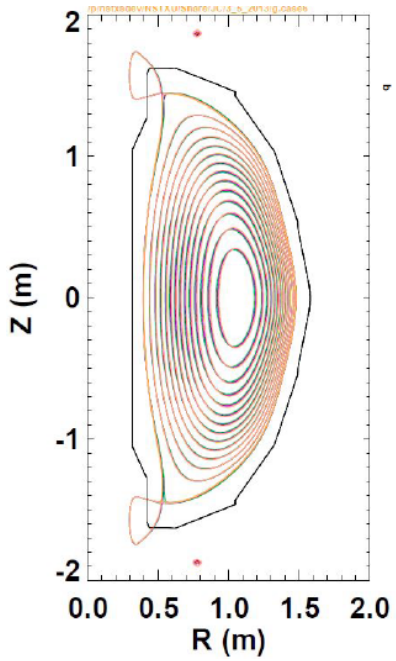

Fig. 5.32: NSTX-U equilibria for the q_{95} scan used in the IPEC study.

The coupling to the dominant external fields for these cases is shown in Fig. 5.30. The coupling magnitudes are similar to those computed for NSTX, especially for the lower q_{95} example. However, at higher q_{95}, the coupling falls off. As a consequence, Fig. 5.31 shows that the displacements at the plasma edge anticipated from 1 kA of current in the antenna are comparable to that achieved in NSTX for q_{95}=6, but become smaller as q_{95} is increased.

Hence, for the present configuration at β_N=4, it is anticipated that the technique will likely only drive large displacements at lower q_{95}. Furthermore, for this family of equilibria, it appears that it may be difficult to drive significant perturbation amplitudes with the existing antenna structure. However, the present cases are stable to n≥4 perturbations, even without a conducting wall. It is anticipated that if the β_N value is further raised, a larger plasma response may occur, potentially facilitating edge control with the HHFW antenna. The β_N dependence of this coupling will be explored in future studies.

Acknowledgement

This research was sponsored by the United States Department of Energy under contracts DE-AC05-00OR22725, DE-FG02-99ER54527, DE-SC0001288, DE-FG02-09ER55012 and DE-AC02-09CH11466.

References

[1] P.T. Lang, et al., Nuclear Fusion **53**, 043004 (2013).
[2] P. T. Lang, et al, Nuclear Fusion **44**, 665 (2004).
[3] P.T. Lang, et al., Nuclear Fusion **47**, 754 (2007).
[4] P.T. Lang, et al., Nuclear Fusion **48**, 095007 (2008).
[5] P.T. Lang, et al., Nuclear Fusion **51**, 033010 (2011).
[6] L.R. Baylor, et al., Phys. Rev. Lett. **110**, 245001 (2013).
[7] A. W. Degeling, et al., Plasma Phys. Control Fusion **45**, 1637 (2003).
[8] P. T. Lang, et al, Plasma Phys. Control. Fusion **46**, L31 (2004).
[9] F. Sartori, et al., *Synchronous ELM Pacing at JET Using the Vertical Stabilization Controller*, 35th EPS Conference on Plasma Physics, Hersonissos, Crete, Greece (2008).
[10] E. de la Luna, et al., "Effect of ELM Mitigation on Confinement and Divertor Heat Loads on JET, paper EXC/8-4, IAEA FEC (2010), Deajeon, Korea.
[11] E. de la Luna, et al., "Magnetic ELM triggering using the vertical stabilization controller in JET", P-5.174, 36th EPS Conference on Plasma Physics (2009), Sofia, Bulgaria.
[12] S.P. Gerhardt, et al., Nuclear Fusion **50**, 064015 (2010).
[13] T. E. Evans, et al., Nature Physics **2**, 419 (2006).
[14] M.E. Fenstermacher, et al., Nuclear Fusion **48**, 122001 (2008).
[15] T.E. Evans, et al., Nuclear Fusion **48**, 024002 (2008).
[16] P.B. Snyder, et al., Phys. Plasmas **19**, 056115 (2012).
[17] K.H. Burrell, et al., Phys. Plasmas **12**, 056121 (2005).
[18] K.H. Burrell, et al., Nuclear Fusion **49**, 085024 (2009).
[19] A.M. Garofalo, et al., Nuclear Fusion **51**, 083018 (2011).
[20] K.H. Burrell, et al., Phys. Plasmas **19**, 056117 (2012).
[21] K.H. Burrell, et al., Nuclear Fusion **53**, 073038 (2013).
[22] W. Suttrop, et al., Plasma Phys. Controlled Fusion **45**, 1399 (2003).
[23] Y. Sakamoto, et al, Plasma Phys. Controlled Fusion **46**, A299 (2004).
[24] N. Oyama, et al., Nuclear Fusion **45**, 871 (2005).
[25] W. Suttrop, et al., Nuclear Fusion **45**, 721 (2005).
[26] F. Ryter, et al., Plasma Phys. Control. Fusion **40**, 725 (1998).
[27] R. McDermott, et al., Phys. Plasmas **16**, 056103 (2009).
[28] D. Whyte, et al., Nuclear Fusion **50**, 105005 (2010).
[29] A.E. Hubbard, et al., Phys. Plasmas **18**, 056115 (2011).
[30] A.E. Hubbard, et al., Nuclear Fusion **52**, 114009 (2012).
[31] J.W. Hughes, et al., Nuclear Fusion **53**, 043016 (2013).
[32] R. Maingi, et al., Journal of Nuclear Materials **390-391**, 440 (2009).
[33] R. Maingi, et al., Phys. Rev. Lett. **105**, 135004 (2010).
[34] D.K. Mansfield, et al., Journal of Nuclear Materials **390-391**, 764 (2009).

[35] F. Scotti, et al., *Core Transport of Lithium and Carbon in ELM-free Discharges with Lithium Wall Conditioning in the NSTX*, submitted to Nuclear Fusion (2013).
[36] D.R. Smith, et al., *Measurements and simulations of low wavenumber pedestal turbulence in the National Spherical Torus Experiment*, submitted to Nuclear Fusion (2013).
[37] J.-K. Park, et al., *Observation of Edge Harmonic Oscillation in NSTX and Theoretical Study of Its Active Control Using HHFW Antenna at Audio Frequencies*, paper EX/P4-33, IAEA Fusion Energy Conference 2012, San Diego, USA.
[38] J.K. Park, et al., *Observation of EHO in NSTX and theoretical study of its active control using HHFW antenna*, submitted to Nuclear Fusion.
[39] D. Boyle, et al., Plasma Phys. Control. Fusion **53**, 105011 (2011).
[40] R.E. Bell, et al., Phys. Plasmas **17**, 082057 (2010).
[41] R.E. Waltz and R.L. Miller, Phys. Plasmas **6**, 4265 (1999).
[42] J. M. Canik, et al., Phys. Rev. Lett. **104**, 045001 (2010).
[43] J.M. Canik, et al., Nuclear Fusion **50**, 064016 (2010).
[44] J.M. Canik, et al., Nuclear Fusion **50**, 034012 (2010)
[45] J.E. Menard, et al., Nuclear Fusion **50**, 045008 (2010).
[46] R. J. Hawryluk, et al., "An Empirical Approach to Tokamak Transport", in Physics of Plasmas Close to Thermonuclear Conditions, ed. by B. Coppi, et al., (CEC, Brussels, 1980), Vol. 1, pp. 19-46.
[47] L.L Lao, Nuclear Fusion **25**, 1611 (1985).
[48] S.A. Sabbagh, et al., Nuclear Fusion **41**, 1601 (2001).
[49] S.A. Sabbagh, et al., Nuclear Fusion **46**, 635 (2006).
[50] J.E. Menard, et al., Phys. Rev. Lett. **97**, 095002 (2006).
[51] B.P. LeBlanc, et al., Rev. Sci. Instrum. **74**, 1659 (2003).
[52] R.E. Bell and R. Feder, Rev. Sci. Instrum. **81**, 10D724 (2009).
[53] D.R. Smith, et al., Rev. Sci. Instrum. **81**, 10D717 (2010).
[54] D.R. Smith, et al., Rev. Sci. Instrum. **83**, 10D502 (2012).
[55] S.P. Gerhardt, et al., Nuclear Fusion **53**, 043020 (2013).
[56] C.S. Chang, S. Ku, and H Weitzner, H. Physics of Plasmas **11**, 2649 (2004).
[57]M. Kotschenreuther *et al*, Comput. Phys. Commun. **88** (1995) 128.
[58] J.M. Canik, et al., "Edge microstability of NSTX plasmas without and with lithium-coated plasma-facing components", Nuclear Fusion at press.
[59] R. Maingi, et al., Nuclear Fusion **52**, 083001 (2012).
[60] M.G. Bell, et al, Plasma Phys. Control. Fusion **51**, 12 (2009).
[61] R. Maingi, et al., Phys. Rev. Lett., **103**, 075001 (2009).
[62] M. Podesta, et al., Nuclear Fusion **52**, 033008 (2012).
[63] F. Scotti, *Modification of impurity sources and transport with lithium wall conditioning in the National Spherical Torus Experiment*, Ph.D dissertation, Princeton University, Department of Astrophysics (2013).
[64] E.A. Belli, et al, Plasma Phys. Control. Fusion **50**, 095010 (2008).
[65] W.A. Houlberg, et al., Phys. Plasmas **4**, 9 (1997).
[66] D.R. Smith, et al., Phys. Plasmas **20**, 055903 (2013)
[67] M. Kutner, et al., *Applied Linear Statistical Models*, 5th ed. (McGraw-Hill, 2005)
[68] Y. Chen and S. Parker, J. Comput. Phys. **220**, 839 (2007).
[69] W. Wan, et al., Phys. Plasmas **18**, 056116 (2011).

[70] A.C. Sontag, et al., Nuclear Fusion **51**, 103022 (2011)
[71] N. Crocker, et al, Plasma Phys. Control. Fusion **53**, 105001 (2011).
[72] P.B. Snyder, et al., Phys. Plasmas **9**, 2037 (2002).
[73] P.B. Snyder, et al., Plasma Phys. Control. Fusion **46**, A131 (2004).
[74] P.B. Snyder, et al., Nuclear Fusion **47**, 961 (2007).
[75] J.-K. Park, et al., Nuclear Fusion **48**, 045006 (2008).
[76] J.-K. Park, et al., Nuclear Fusion **51**, 023003 (2011).
[77] J.-K. Park, et al., Phys, Plasmas **14**, 052110 (2007).
[78] S.P. Gerhardt, et al., Nuclear Fusion **52**, 083020 (2012).